DENSIFICATION AND PROPERTIES EVOLUTION OF STAINLESS STEEL ALLOYS FABRICATED BY THREE-DIMENSIONAL PRINTING

By:

YONGHA KIM

A thesis submitted in partial fulfillment of
the requirements for the degree of

Master of Science in Mechanical Engineering

WASHINGTON STATE UNIVERSITY
School of Engineering and Computer Science

August 2009

To the Faculty of Washington State University:

The members of the Committee appointed to examine the thesis of YONGHA KIM find it satisfactory and recommend that it be accepted.

_____
Dae-Wook (Dave) Kim, Ph.D., Chair

_____
Stephen Solovitz, Ph.D.

_____
Wei Xue, Ph.D.

ACKNOWLEDGMENT

The author wishes to acknowledge Professor Dae-Wook (Dave) Kim, PhD for his countless hours of guidance, wisdom, and support for the research; Li Sun and Professor Patrick Kwon at Michigan State University for their collaboration.

DENSIFICATION AND PROPERTIES EVOLUTION OF STAINLESS STEEL ALLOYS FABRICATED BY THREE-DIMENSIONAL PRINTING

Abstract

By Yongha Kim, MS
Washington State University
August 2009

Chair: Dae-Wook (Dave) Kim

Solid Freeform Fabrication (SFF) techniques are novel manufacturing processes that fabricate parts directly from Computer-Aided Design model with layer-by-layer fashion in short lead time. Because of those characteristics, SFF have such advantages as great manufacturability for complex-shaped parts, short manufacturing lead time, and low manufacturing cost for some of SFF techniques. However, there are also disadvantages such as limited material selections, dimensional error, and low relative density of SFF processed parts.

Among various SFF techniques, three-dimensional printing (3DP) has advantages of low manufacturing cost and short lead time over other SFF techniques such as stereolithography, fused deposition modeling and selective laser sintering. However, low density and mechanical properties of the 3DP products have been issues for 3DP technology to expand their applications. This study is aimed to investigate the effect of adding Si_3N_4 on the density and properties evolution of three-dimensional printing (3DP) processed 420 stainless steel (SS) parts. The final density, dimensional changes, and mechanical property have been studied for the samples after a series of sintering conditions. The contents of Si_3N_4 powder ranging between 0 and 15 wt% and the sintering temperature were varied in the experiments in order to understand the dependence of densification kinetics and properties changes on these process parameters. The experiments provide the evidence that the addition of Si_3N_4 can improve the densification kinetics of 420 SS

significantly. The 420 stainless steel samples produced by 3DP with 12.5 wt% Si_3N_4 sintered at 1225 ℃ for 6 hours yielded 95% relative density, 190GPa Young's modulus, and 500 Knoop microhardness without any major sample shape distortion. The results are promising in that the 3DP process can be used to yield the prototype almost equivalent to a real part with a full mechanical capacity.

TABLE OF CONTENTS

Page

LIST OF TABLES

LIST OF FIGURES

Dedication

This thesis is dedicated to my wife Youngmi Hong, my son Daniel Kim, and the second one coming to us, and also dedicated to my parents and parents in law for their supports.

CHAPTER ONE

INTRODUCTION

Since the first commercial solid freeform fabrication (SFF) system was presented at the AUTOFACT show in Detroit, MI in 1987 [1], this technology has been recognized as the most flexible method to fabricate prototypes with complex structures in near net shape directly from computer-aided design (CAD) models of those components. Utilizing the sliced cross-sectional data transformed from three-dimensional CAD data, SFF parts are built up physically in a layer-by-layer mode. Because SFF techniques can fabricate parts with complex geometry in relatively shorter lead time than that of conventional manufacturing technologies, they have been increasingly used in all sectors of engineering industries for rapid fabrication of prototypes and products to manufacture challenging designs [2].

The SFF technologies were further developed through the 1980s and 1990s, which resulted in the commercially successful technologies such as Stereolithography Apparatus (SLA), Fused Deposition Modeling (FDM), Selective Laser Sintering (SLS), and Three-Dimensional printing (3DP).

SLA technique uses local photo curing of specially developed liquid polymer materials to build structures. FDM employs the computer numerically controlled extrusion and rapid cooling of molten thermoplastic materials to fabricated parts. SLS utilizes modulation of a focused laser to selectively sinter or fuse powdered materials for the fabrication of parts. 3DP, which is used in this research, is powder-based technique similar to that of SLS, but it uses polymeric binder material from an inkjet printer head to hold powder in order to build structures [3]. Inkjet printer head prints a liquid binder phase onto the powder layer in a designed cross-sectional shape. Then, an additional layer of powder is spread onto the exiting binder/powder layer. The printing process is repeated till all of the required layers are printed and stacked [4,5,6].

Even though SFF techniques are novel and they have abilities of fabricating complex shape quickly, there are some issues need to be improved such as limited material selection, rough surface finish, dimensional error, and poor mechanical properties [7]. One of the most challenging tasks for production using SFF technologies is to have sound mechanical properties with satisfying dimensional accuracy. Most Rapid Prototype (RP) products have far less than 100% theoretical density, which causes poor mechanical properties. For specific, 3DP green parts contain open void of up to 30% by volume and its relative density is typically about 50% – 60%. Because the powders are loosely deposited in 3DP, the sintered 3DP parts often have the relatively lower density than that of the sintered powder metallurgy parts. Therefore, expensive additional post-processes such as infiltration and isostatic pressing are required to increase the density of 3DP [6].

The objective of this study is to improve the final density of the stainless steel parts in order to enhance mechanical properties produced by the 3DP method without additional post-processes. This particular study investigated the effect of adding Si_3N_4 on the density and dimensional changes and mechanical properties of the 3DP processed 420 stainless steel workpieces in a series of sintering conditions.

This thesis is composed of six chapters. The first Chapter, the Introduction, provides some general information about some of the topics that will be discussed in this report. The Literature Review, Chapter 2, provides additional depth about topics significant to the direction of this report and provides details as to past and present research in relevant areas. Chapter 3, the objectives, concisely explains the reason for this research and the goals that were established at the onset of this study. Chapter 4 informs the reader of the procedures and equipment used during all experimental analysis in this work. Next, Chapter 5 presents the results obtained from the experimental work and also provides a discussion of these results. Finally, Chapter 6 establishes conclusions from this study and recommends future study topics.

CHAPTER TWO

LITERATURE SURVEY

2.1 SOLID FREEFORM FABRICATION TECHNOLOGIES

Basic principles of how to fabricate the parts from a variety of Solid Freeform Fabrication (SFF) techniques can be included in following two factors [8]:

1) Parts are fabricated directly from the CAD models;

2) Layer by layer fashioned manufacturing;

Those characteristics make it possible to produce the final parts with arbitrary geometries from CAD models, so that SFF techniques are widely used in diverse fields of industry [8]. Recently, SFF techniques are widely employed to manufacturing microstructures and biomedical components.

There are four most popular SFF technologies as shown below.

- Stereolithography Apparatus (SLA)
- Fused Deposition Modeling (FDM)
- Selective Laser Sintering (SLS)
- Three-Dimensional Printing (3DP)

In following sections, the detailed descriptions on four representative technologies' principle, process, applications, and current research directions are described.

2.1.1 Stereolithography Apparatus (SLA)

SLA technique is the first SFF technique reported by Chuck Hull in 1986 [9]. The prefix 'stereo' refers to three-dimensional quality, and 'lithography' is the name of an ancient printing technique. SLA technique uses UV radiation from a laser for the polymerization of photo-curable liquid monomers [1]. Photo-curable liquid monomers contain 2-5% photo initiators that produce free radicals in the existence of UV light. When the UV light scans the surface of liquid monomer, polymerization occurs due to the attacks of generated free radicals on monomers [10], and one layer is solidified. Once the first layer is completed, which is attached to the support platform, then the support platform goes down to the depth of layer thickness and prints another layer [8]. This process is continued until the final part is fabricated. Fig. 2.1.1-1 [11] shows the process of SLA. Once the fabrication process is completed, the support platform is elevated and the supports are removed, and then post-curing process in UV oven is followed [8,12].

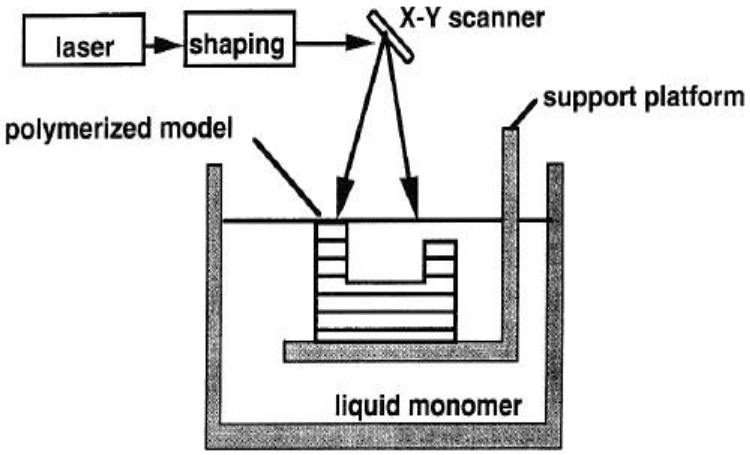

Figure 2.1.1-1. Schematic of SLA technique for fabrication of three-dimensional objects. [11]

SLA technique has been used for various applications including investment casting and conceptual modeling. In particular, because of the high accuracy of the SLA process, and the translucency and density of the final parts, SLA has been used for the medical and dental modeling applications to create skeletons or jaws to improve surgical planning as shown in Fig. 2.1.1-2, b) and c) [8,13,14]. 3D CAD models for prototyping can be obtained from individual patient-data such as CT scan and MRI data. [15]. As well as modeling applications, SLA parts can be used as actual parts for tissue engineering and biomedical engineering applications. Schuster et al. [16] have produced 3D structures from biodegradable photopolymers for hard tissue replacement. Since micro-SLA technique was introduced in late 90's [17], micro-sized features have been fabricated with extremely high resolution as shown in Fig. 2.1.1-3. For biomedical applications, Lee et al. [18] and Kim et al. [19] used biodegradable (Poly Propylene Fumarate / Diethyl Fumarate) and biocompatible (Hydroxyapatite nanopowdder) materials respectively to fabricate 3D scaffolds. Although those biodegradable and biocompatible phothopolymers have been arranged for the replacement of cellular bone, SLA has not yet been utilized to fabricate the parts for implants. This is because leachates from under-cured polymers can cause toxic reactions [14], which are not desired. Therefore, commercialization of SLA parts for the biomedical applications is still an on-going research topic.

a) b) c)

Figure 2.1.1-2. Applications of SLA: a) Pattern for investment casting, b) Skull, and c) Jaw prototypes for surgical planning, [8,13].

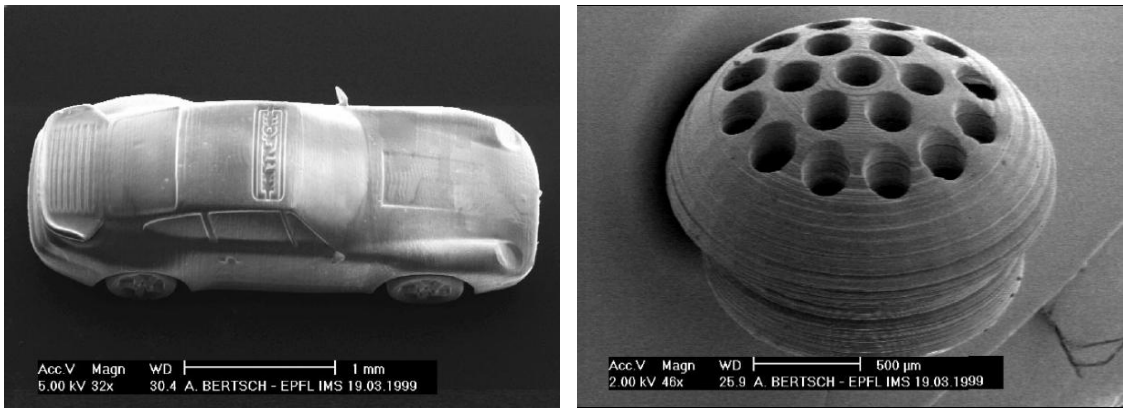

a) b)

Figure 2.1.1-3. Micro-sized features fabricated by SLA: a) Car model with layer thickness of 5µm, b) Part of hearing aid [19].

A SLA technique has been also employed to fabricate ceramic structures and metal/polymer composite structures. For the ceramic structures, photo-curable polymers act as a binder for the ceramic powder and removed with high temperature where ceramic powders are sintered [10]. Professor Halloran [10] at University of Michigan fabricated a ceramic electromagnetic band-gab structure with resolution of about 100µm and Zhou et al. [20] fabricated nickel-coated SLA aircraft model with complex geometry to make use of advantages from both SLA technique and mechanical properties from metal materials.

SLA is now being widely used in a variety of fields due to its own characteristics such as high accuracy and great surface finish as mentioned in this section.

2.1.2 Fused Deposition Modeling (FDM)

Fused Deposition Modeling, as shown in Fig. 2.1.2-1, was first developed by Scott Cramp in 1988, and commercialized by Stratasys Inc. [21]. It utilizes a temperature-controlled head to extrude thermoplastic polymer from the nozzle, and draw a model with melt plastic in semi-liquid state one layer at a time. After printing the first layer, a movable platform moves down at an interval of layer thickness to draw another layer, and those steps are repeated until the parts are completed. The thermoplastic material deposited on the printing layer is cooled and solidified immediately after being extruded, so that the deformation and distortion of the parts can be minimized. The entire extrusion processes are performed in a chamber at just below melting temperature of thermoplastic polymer material [8].

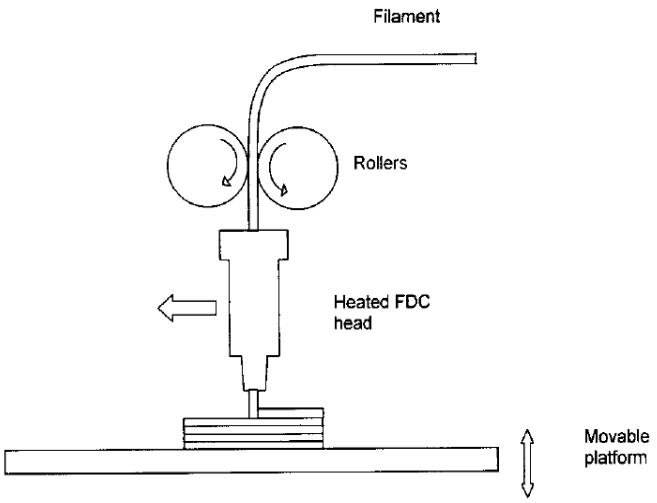

Figure 2.1.2-1 Schematic diagram of fused deposition modeling process [10]

FDM system can fabricate a fully functional parts such as Acrylonitrile Butadiene Styrene plastic (ABS, light and rigid properties) parts in relatively short lead time without any post processing such as de-binding and sintering. The final ABS parts have 85% of the strength of the actual molded parts. Therefore, the parts from the FDM can be utilized for actual testing, especially for consumer products [21]. For instance, Toyota, one of the largest automobile

manufacturers in the world, is using FDM techniques to enhance their design efficiency and testing capability. In the Avalon 2000 project, Toyota adapted FDM system rather than conventional tooling method on 35 parts, and saved tooling costs of $2 million [21].

While FDM technique became very popular in automotive and electronics consumer product design and manufacturing, current researches on FDM have been performed for the biomedical applications. Zeng et al. [22] fabricated an auricle framework for microtia reconstruction with thermoplastic polyurethane material because of its good flexibility and biocompatibility. Kouhi et al. [23] designed and manufactured reconstructive mandibular models by FDM method for assisting in the planning of surgery. Yamada et al. [24] tried to fabricate 3D microstructures by means of FDM technique using biodegradable polylactide polymers with high resolution of 40μm and biocompatibility as shown in Fig 2.1.2-2., as possible applications for micro-sized implantation. Polymer-ceramic composite scaffolds were fabricated by Kalita et al. [25] with polypropylene (PP) and tricalcium phosphate (TCP) for bone grafts applications to achieve plasticity and processibility of bone structures.

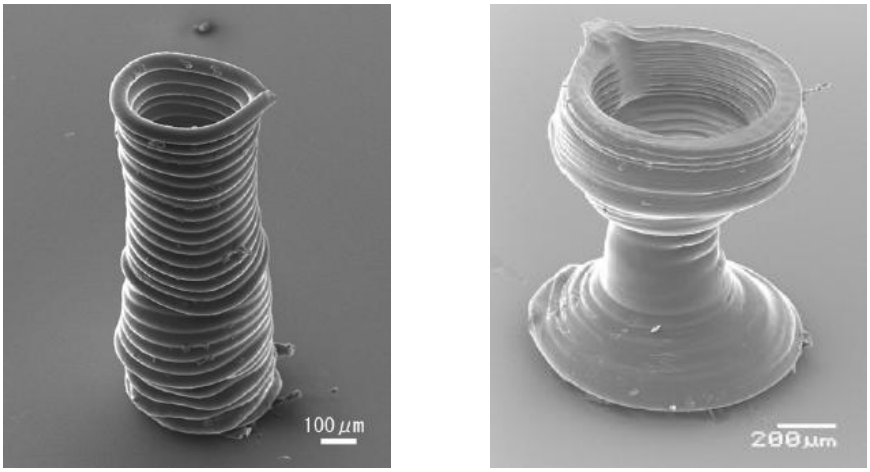

a) b)

Figure 2.1.2-2. SEM images of a) micro-pipe and b) micro-wine glass with a high resolution of about 40μm fabricated by FDM [24].

Even though a FDM technique is polymer extrusion based technique, it is also possible to fabricate metal or ceramic parts by using basic principles of FDM technique. Finke and Feenstra [26] developed a metal fabrication system by extrusion and deposition of semi-solid alloys to take an advantage of absence of post processing in FDM process. Allahverdi et al. [27] created electroceramic transducers with bismuth titanate powder as shown in Fig. 2.1.2-3. Thermoplastic polymer was used as a binder for ceramic powder, so that post processes such as eliminating polymer material and sintering or, in some cases, infiltration were required. FDM method for ceramic process has advantages of fast fabrication with low cost even though several post processed are followed.

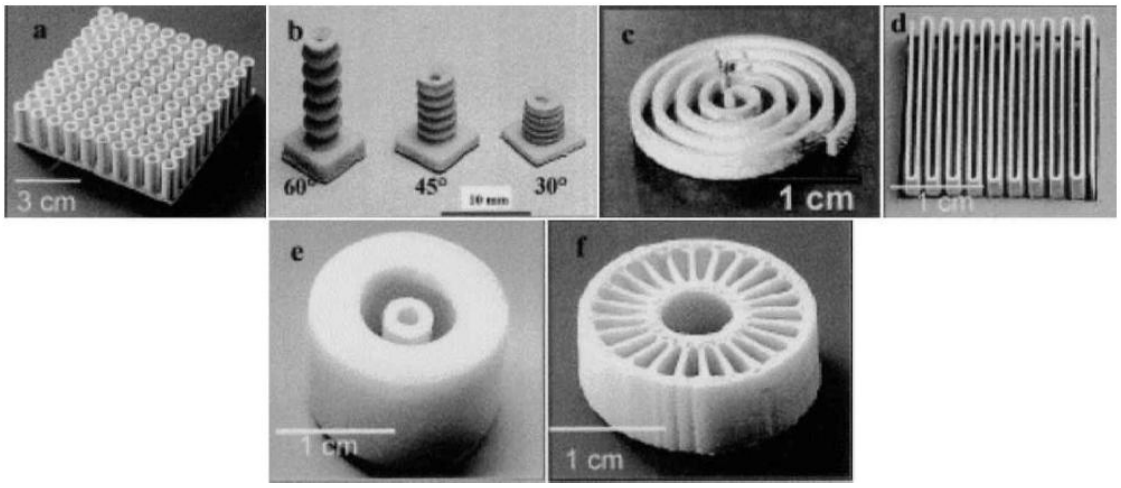

Figure 2.1.2-3. Electroceramic transducers created by FDM method [27]

2.1.3 Selective Laser Sintering (SLS)

Selective laser sintering technique was developed by Carl Deckard at the University of Texas at Austin in 1986 and commercialized in 1992 [10]. SLS technique fabricates parts by sintering powdered materials using laser beam energy. The powdered material is spread by a roller over the fabricating bed which a laser beam is directed. A laser beam selectively traces an area as defined by the geometry of the cross-section of a CAD model to fuse materials by sintering or melting. When the first layer is completed, the fabrication stage moves down to the depth of layer thickness, and powder material is provided by a roller from another bed, supply bed, for the sintering or melting an area of the next layer of 3D parts. These procedures repeated until final parts are completed [8]. If melting occurs rather than sintering on the surface of powdered materials because of a high intensity laser, the manufacturing process is called Selective Laser Melting (SLM).

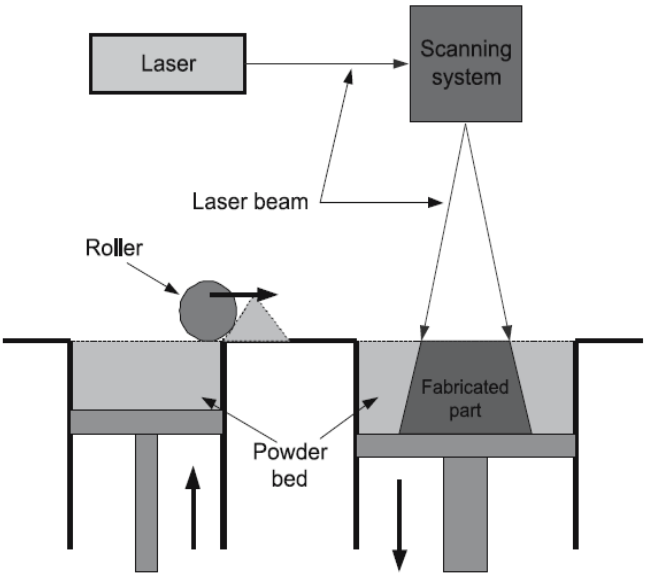

Figure 2.1.3-1. Schematic of SLS process [8]

By using SLS or SLM, it is possible to fabricate parts from a variety of materials such as polymers, metals, and ceramics. Especially, SLM allows fabricating 100% density parts without post processes because of elimination of void by melting process, and thus it would also enhance mechanical properties of final parts. Elimination of post processes also contributes to saving manufacturing time [28,29]. Due to its advantages including diverse material selections and high dense final parts, many end-use metallic products with challenging shapes have been produced in industries. For example, Boeing has used SLS to make parts for the International Space Station project [30].

Taking an advantage of SLM's high dense parts fabrication capability with ceramic materials, Clare et al. [31] fabricated full dense 3D nickel-titanium shape memory alloy (SMA) structures by SLM for MEMS applications, which is very hard to be achieved by any other SFF techniques with ceramic homogeneous materials.

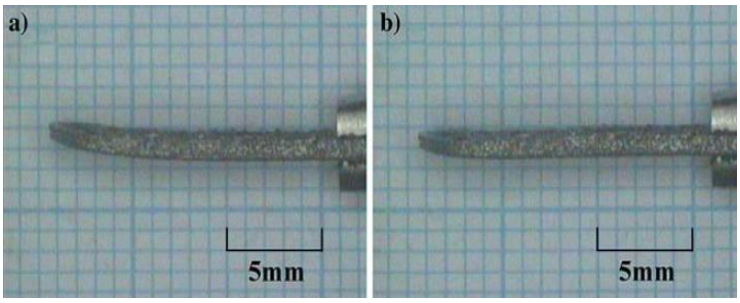

Figure 2.1.3-2. Two Way Trained NiTi Cantilever Beams a) shows the low temperature martensitic phase b) shows the high temperature austenitic phase [31].

Besides such advantages as diverse material selections and high dense final parts, SLS and SLM can fabricate metal or ceramic parts with high resolution. Using SLM's high resolution capability, Yadroitsev et al. [32] fabricated fine-structured 3D filter elements using 316L stainless steel powder with the size of channel of about 150μm × 150μm, as shown in Fig. 2.1.3-3. For the smaller-sized channel fabrication than 150μm × 150μm, the channels are often closed, causing irregular mat structure [32].

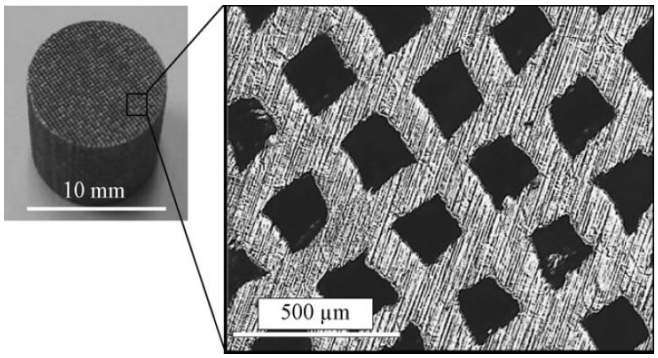

Figure 2.1.3-3. Filter from 316L stainless steel with micro-sized channels by SLS [32]

By using chemical reactions during SLM process, Shen et al. [33] fabricated 316L stainless steel structure with micro-sized (average in 2µm) pores for possible heat exchanger and cooling machine application. By adding additive materials (H_3BO_3 and KBF_4), they induced chemical reactions during SLM process to generate gases to fabricate pore structures, as shown in Fig. 2.1.3-4. For a biomedical application, SLS technique was employed to fabricate custom-made bioactive structures with hydroxyapatite and polyamide composites by Savalani et al. [34].

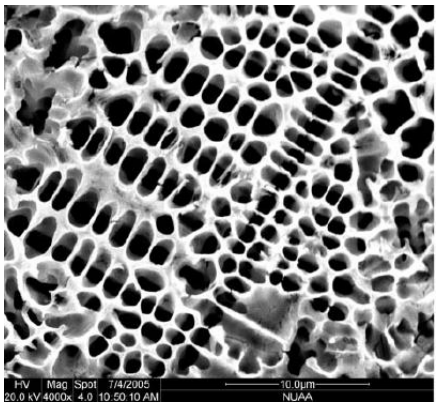

Figure 2.1.3-4. SEM image of SLM processed porous 316L stainless steel (scale bar represents 10µm) [33].

In spite of relatively high manufacturing cost, SLS and SLM are widely employed to a variety of applications due to their own characteristics as described above.

2.1.4 Three-Dimensional Printing (3DP)

Three-dimensional printing was developed at Massachusetts Institute of Technology in 1992 [35]. As shown in Fig. 2.1.4-1 [35]. 3DP technology fabricates parts by spreading thin layer of powder and applying binder with an ink-jet printhead on the desired cross sectional geometry of the parts. When the first layer is completed, then the printing stage descends to the depth of layer thickness, and powder material is provided from supply bed. The parts are fabricated by repeating the processes of spreading power layers and printing the desired patterns of binder material until the parts are completed [6].

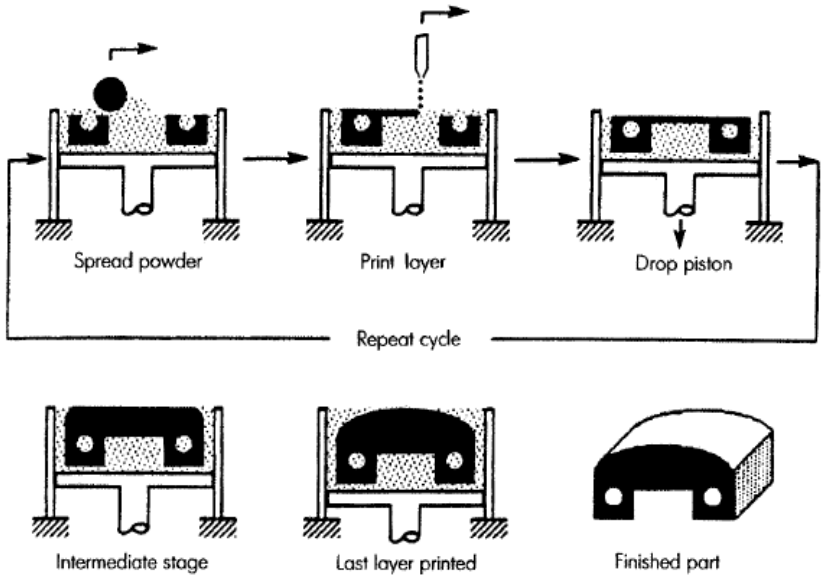

Figure 2.1.4-1. Schematic diagram of three-dimensional printing method [35].

According to Bak [36], the main advantage of 3DP is its faster manufacturing speed than that of SLS and SLA for small production volumes. In addition, freedom of material selection, great manufacturability especially for complex part geometries as shown in Fig. 2.1.4-2., and low manufacturing cost are advantages of 3DP technique [6].

a) b)

Figure 2.1.4-2. Complex 3D printed parts: a) A gear shift boot [37], and b) an architectural model [38]

3DP can be widely used in diverse manufacturing fields. First of all, metal tooling can be fabricated by printing with 420 stainless steel powder, and sintering and infiltrating with bronze material for sound mechanical properties [6]. For automotive application, Dimitrov et al. [37] fabricated rubber similar parts for a gear shift boot, as shown in Fig. 2.1.4-2 a), for the purpose of noise reduction. Starch based powder was used for the printing and infiltrated with a polyurethane rubber molding system in lead time of 5hours [37].

3DP is recently used not only for traditional metal processing, but also for fabrication of multifunctional composites and functionally graded materials. Sun et al. [39] fabricated high dense multifunctional composite with Ti_3SiC_2 which possesses unique properties from metals and ceramics such as mechanical strength, high electrical and thermal conductivities [40,41]. Kaczynski [42] reported that the parts with functionally graded materials can be fabricated by 3DP. Using local composition control technique by means of control of a multi-material printhead, composition of a part can be controlled.

In medical field such as surgical aids and organ printing, 3DP is widely used. In terms of manufacturing cost for surgical aids, a 3DP part is less than a SLA part by as much as 50%, so that 3DP has been increasingly used for surgical aids purposes [38].

While 3DP is very versatile fabrication technique as mentioned above, there are some weaknesses needed to be improved as listed below [38], and currently those are still good topics for the 3DP related researches.

- Inaccuracy of parts compared to those of other SFF techniques
- Poor surface finish
- Limited material selection compared to SLS/SLM
- Need of one or two secondary stages such as sintering and infiltration due to porosity.

2.2 DENSIFICATION OF 3D PRINTED WORKPIECES

The advantages of 3DP technology such as versatility in manufacturing, short lead time, and low manufacturing cost are described in section 2.1.4, and also disadvantages are explained. Among disadvantages of 3DP process, porosity of the 3D printed part is one of the challenges because it causes poor mechanical properties of the final parts.

In order to achieve high dense 3D printed parts, various attempts such as infiltration, post-processing, and powder selection have been made. Infiltration techniques use liquid-state metals or alloys to be absorbed into the porous structures. Other than infiltration methods, some post-processes such as Hot Isostatic Pressing (HIP) and Cold Isostatic Pressing (CIP) were applied to induce shrinkage by pressure. Furthermore, some researchers used extremely fine powder to obtain parts with high relative density.

In the following sections, the detailed descriptions on densification processes such as infiltration, post isostatic pressing, and use of fine powder method are described.

2.2.1 INFILTRATION

Liquid-metal infiltration process has been considered as one of the most common ways to achieve denser 3DP parts. The principle of the infiltration process is that the infiltrant are filled with the void portion of the parts by capillary force caused by surface tension of powders as shown in Fig. 2.2.1-1. [43]

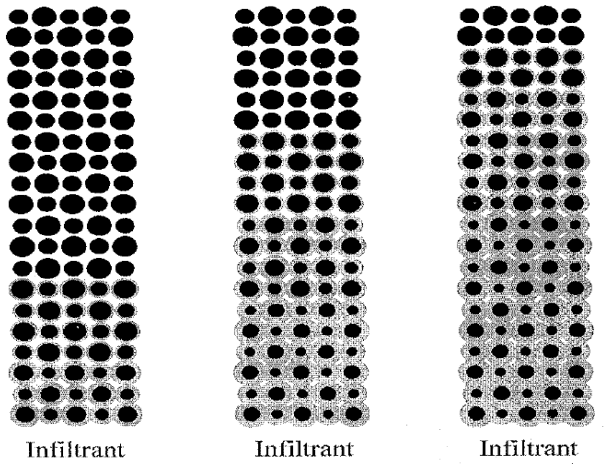

Figure 2.2.1-1. Schematic illustration of infiltration process according to the time sequence [43]

For a tooling application, in order to fabricate tools with good hardness and wear resistance, 420 stainless steel powder is well used as a skeleton materials, and bronze (Cu with 10wt% Sn) is widely used as a suitable infiltrant for the liquid-metal infiltration of 3D printed tools [6]. Liquid-metal infiltration process offers very small dimensional changes (about 2% linear shrinkage), but there are three requirements for the selection of infiltration materials: [6]

1) Melting point of the infiltrant should be lower than that of main powder materials.
2) The components of main powder materials should not be dissolved in the infiltrant.
3) Infiltrant should be strong enough to be utilized for tooling applications.

In order to create a high-dense homogeneous metallic 3DP parts, Lorenz et al. [44] used transient liquid-phase infiltration. Transient liquid-phase infiltration has been considered as a novel alternative for densification of 3DP parts because homogeneous final parts can be fabricated without significant dimensional change [44].

a)

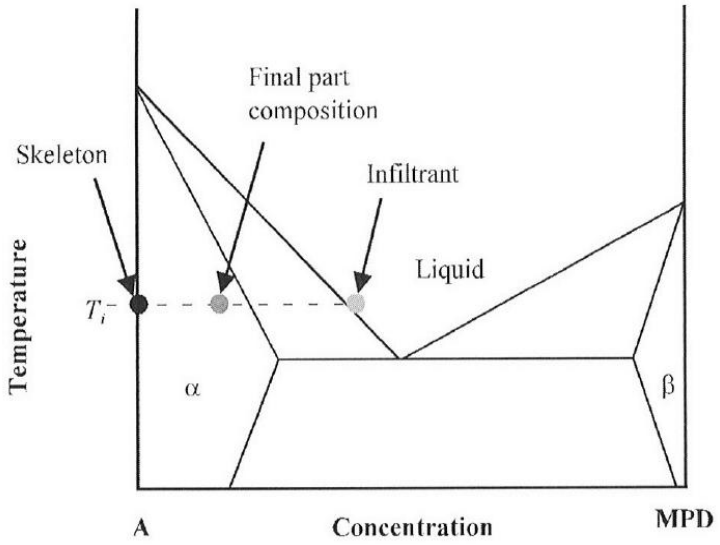

b)

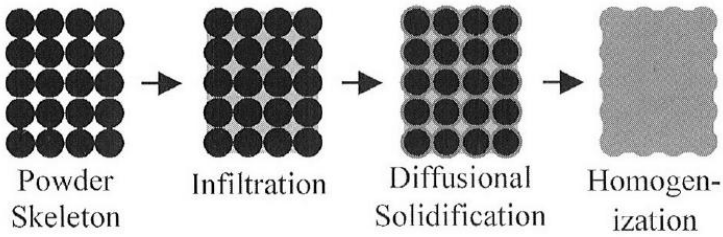

Figure 2.2.1-2. a) Phase diagram and b) schematic illustration for the explanation of transient liquid-phase infiltration mechanism [44]

The particular infiltrant they used for transient liquid-phase infiltration contains components of the 3DP green material as well as a melting-point depressant. Presence of melting-point depressant makes it possible to generate liquid-phase in the material system at lower than meting temperature of skeleton material, and that liquid-phased material is infiltrated in the void

space of the 3DP parts. After the infiltration process, the infiltrated liquid-state material diffuses into the solid skeleton material to be an equilibrium state, causing homogenization as shown in Fig. 2.2.1-2 [44].

Nickel based alloy was fabricated by 3DP, and Si of 4wt% was used as a melting-point depressant by Lorentz et al. [44]. They fabricated 8 samples to compare the effects of different post processes as shown in Table 2.2.1-1. Sample A and B are immediately cooled after transient liquid-phase infiltration, and Sample C and D are homogenized after infiltration at 1200°C for 5hours, and Sample E and F are hot isostatic pressed after homogenization. It can be found from the results that transient liquid-phase infiltrated samples or homogenized samples with infiltration can have about a half ultimate tensile strength of casted samples. Hot isostatic pressing process significantly enhanced mechanical properties of infiltrated or homogenized samples such as ultimate tensile strength and ductility, up to the level of casted samples. From maximum strain results from samples A, B, C, and D, it can be found that homogenization improved ductility of infiltrated samples by over than 30%.

Table. 2.2.1-1. Tensile test results for samples of Ni with 4wt% Si [44].

Sample	Condition	Elastic Modulus (GPa)	Yield Stress (MPa)	UTS (MPa)	Max Strain (Pct)
A	infiltrated	230	156	250	4.6
B	infiltrated	200	184	230	1.4
C	homogenized	275	133	230	6.4
D	homogenized	220	118	201	4.1
E	hot isostatic pressed	200	200	423	34
F	hot isostatic pressed	210	152	436	41
G	cast	400	123	400	30
H	cast and homogenized	210	162	370	64

2.2.2 POST ISOSTATIC PRESSING

By Post Isostatic Pressing (PIP) before or after sintering process, it is also possible to achieve almost full density of final 3D printed parts. In PIP processes, the porous parts compressed with equal force in all directions, and depending on the process temperature, it can be divided into Cold Isostatic Pressing (CIP) and Hot Isostatic Pressing (HIP). The process temperature of CIP is normally in room temperature and that of HIP is above 1000°C [45]. Using CIP before sintering process with a profile as shown in Fig. 2.2.2-1 b), Sun et al [39] fabricated high dense multifunctional composite with Ti_3SiC_2, which has mechanical strength, and high electrical and thermal conductivities. By applying CIP process, final density values were increased by 25% to 30%, and maximum density value obtained was about 95% of full density.

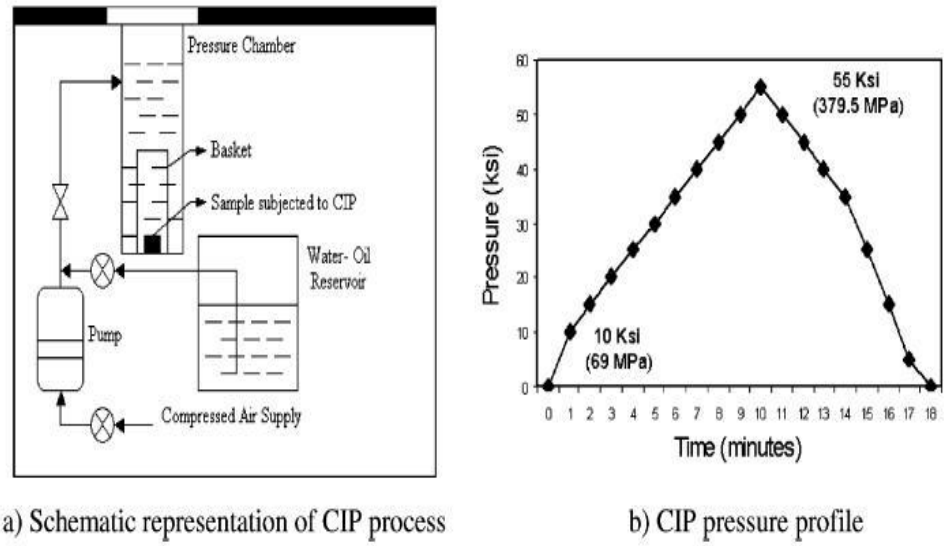

a) Schematic representation of CIP process

b) CIP pressure profile

Figure 2.2.2-1. Schematic representation of CIP and the profile [39].

Sicre-Artalejo et al. [46] produced Inconel 718 parts with the final relative density of 97% using HIP process. 3D printed parts first were sintered at 1300°C. After sintering, HIP at 1200°C with the pressure of 142MPa, and at 1210°C with the pressure of 206MPa was applied for 3 hours to achieve full density.

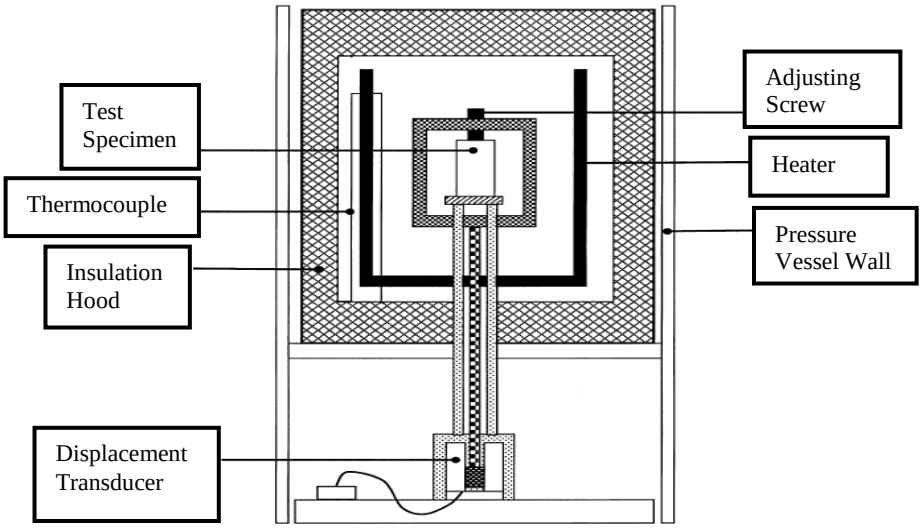

Figure 2.2.2-2. Schematic representation of HIP process [47]

2.2.3 USE OF FINE POWDER

Recently, a few efforts have been made to improve the final density of 3DP parts with use of fine-sized powder. Kakisawa et al. [5] manufactured 3DP parts made by an extremely fine powder of 5 μm, and obtained relative density of 92% for nickel parts. Using stainless steel powder, Godlinski et al. [48] also used fine sized powders to manufacture dense stainless steel parts. In addition, Lanzetta and Sachs [49] used different sized alumina powder, which called bimodal powder, firstly to improve surface finish. But as a bi-product, increased packing density was obtained by filling up voids with small-sized particles (4μm alumina powders) as shown in Fig. 2.2.3-1. b).

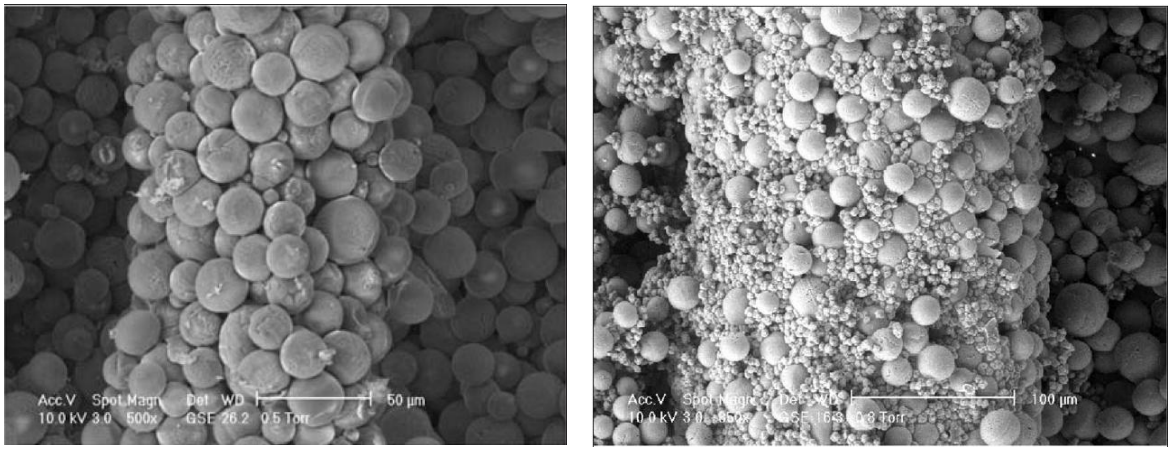

a) b)

Figure 2.2.3-1. 3D printed wire structures: a) with 20μ alumina powder, and b) with 20μ and 4μm alumina powders [49].

2.3 Fabrication of Micro-sized Structures using 3DP

Fabricating micro-sized structures using 3DP technique is a challenging task due to their fragility of green parts. Powders in green parts are temporarily connected with solidified polymeric glue, so that the strength of green parts is very weak. Therefore, fabricating microstructures by means of 3DP is very challenging, so that only a few researches can be found. Research teams [67, 68] at Virginia Polytechnic Institute and State University performed researches to fabricate fine-meshed structures with shape memory alloy material (TiNiHf) and investigated the effect of powder size and 3DP process parameters such as binder saturation and layer thickness on final feature of 3D printed parts. Binder saturation percentage is expressed by binder volume deposited over void volume available [69]. Fig. 2.3-1 shows the 3D CAD design of fine mesh structure and fabricated samples with different 3DP process parameters, and Fig. 2.3-2 shows a 3D fine mesh structure with optimum 3DP process parameters, binder saturation of 170% and layer thickness of 35μm. Powder size (average in less than 20μm) was an independent variable for the research of process parameter effects.

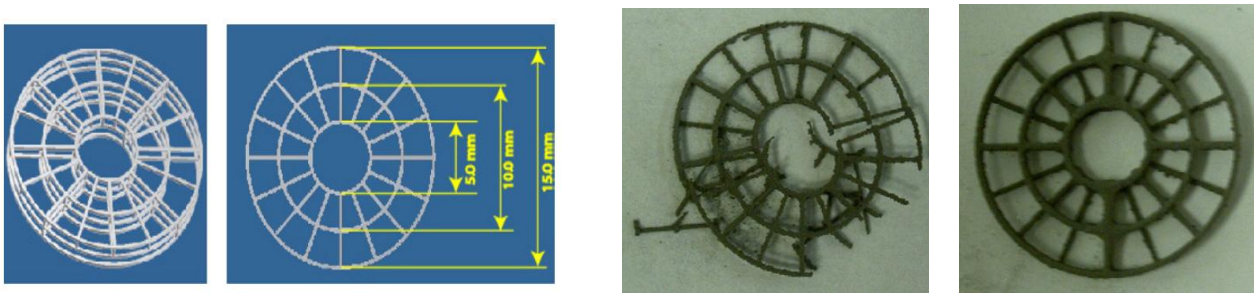

a) b) c)

Figure 2.3-1. a) Designed 3D mesh structure, Fabricated 3D mesh structures with layer thickness of 50μm and binder saturation of a) 55% and b) 170% [67].

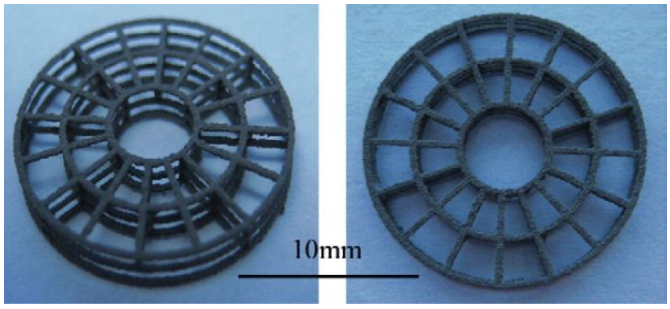

Figure 2.3-2. 3D fine mesh structure with optimum 3DP process parameters, binder saturation of 170% and layer thickness of 35μm. Powder size: average in less than 20μm [67].

For the powder size effect assessment, smaller powder size offers higher green strength of mesh structure, as shown in Fig. 2.3-3 [68], which is desired for handling green samples.

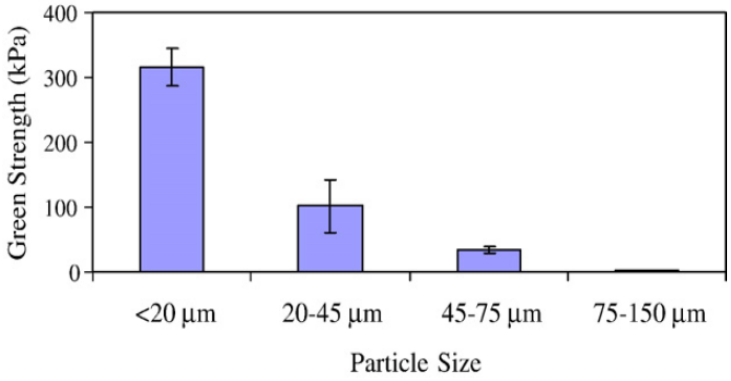

Figure 2.3-3. Green strength of 3D mesh structures from four different size TiNiHf paticles [68].

CHAPTER THREE

RESEARCH OBJECTIVES

One of the most attractive characteristics of 3DP is an excellent manufacturability in short lead time. The drawback of 3DP is low relative density of final parts which is less than 60% typically. Because of that shortcoming, mechanical properties of 3D printed parts are also poor. Different kinds of infiltration methods or post processes can be applied to increase the final density, but those post processes increase the cost of whole process.

In this work, increasing relative density and mechanical properties of 3D printed parts without major shape distortion were the major targets, with the method of mixing metal (420 stainless steel and ceramic powder (Si_3N_4), because it has been found that the addition of Si provides a condition for liquid eutectic activated sintering process in stainless steel [58, 70], so that high relative density of final parts can be achieved.

The following are the goals of this research:

1) Fabricate high dense metallic parts using 3DP technology.
    - Add Si_3N_4 to generate transient liquid phase during sintering
    - Investigate the behavior of relative densities

2) Investigate the property evolution of 3DP processed SS parts with varying Si_3N_4 and sintering temperature.
    - Investigate mechanical properties evolution
    - Investigate shape maintenance capability

CHAPTER FOUR

EXPERIMENTAL DESIGN AND PROCEDURES

4.1 MATERIALS

4.1.1. MARTENSITIC 420 STAINLESS STEEL (420 SS)

Martensitic 420 stainless steel (420 SS) is a hardenable, straight-chromium steel, which combines superior wear resistance with excellent corrosion resistance. Typical applications of 420 stainless steel include surgical and dental instruments, shear blades, and oil extraction components. The spherical 420 SS powder (Exone, USA) was chosen for the experiments and its contents are shown in Table 4.1.1-1, and particle appearance and distribution profile are shown in Fig. 4.1.1-1 and Fig. 4.1.1-2, respectively. The particle size distribution of 420 SS ranges between 22 to 53 μm with the mean size of 35 μm. These values are provided by the manufacturer of each powder.

Table 4.1.1-1. Chemical compositions of 420 SS

C	Si	Mn	P	S	Cr	Ni	Mo	N	Fe
0.43%	0.52%	0.32%	0.017%	0.008%	13.6%	0.47%	0.14%	0.110%	84.385%

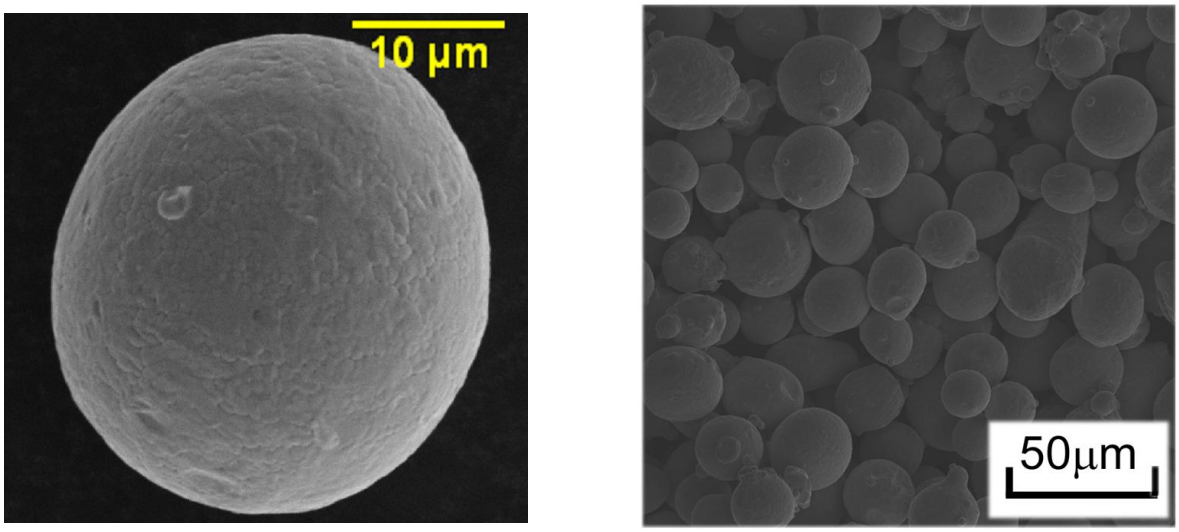

Figure 4.1.1-1. Appearance of 420 SS powder

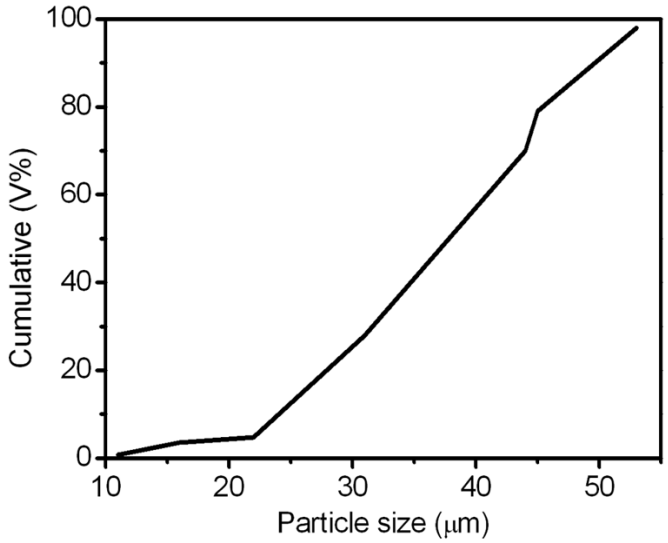

Figure 4.1.1-2. Size distribution of 420 SS powder

4.1.2. Si_3N_4 POWDER

Si_3N_4 powder (Denka, Japan) was chosen to increase density of the 3DP parts. The particle size distribution of Si_3N_4 powder was measured by the Malvern Mastersizer Micro (Malvern Instruments, UK) with 0.4% Nonidet-P40 as the dispersant and its range is 1 to 35 μm with the mean size of 2 μm. Particle appearance and distribution profile are shown in Fig. 4.1.2-1 and Fig. 4.1.2-2, respectively.

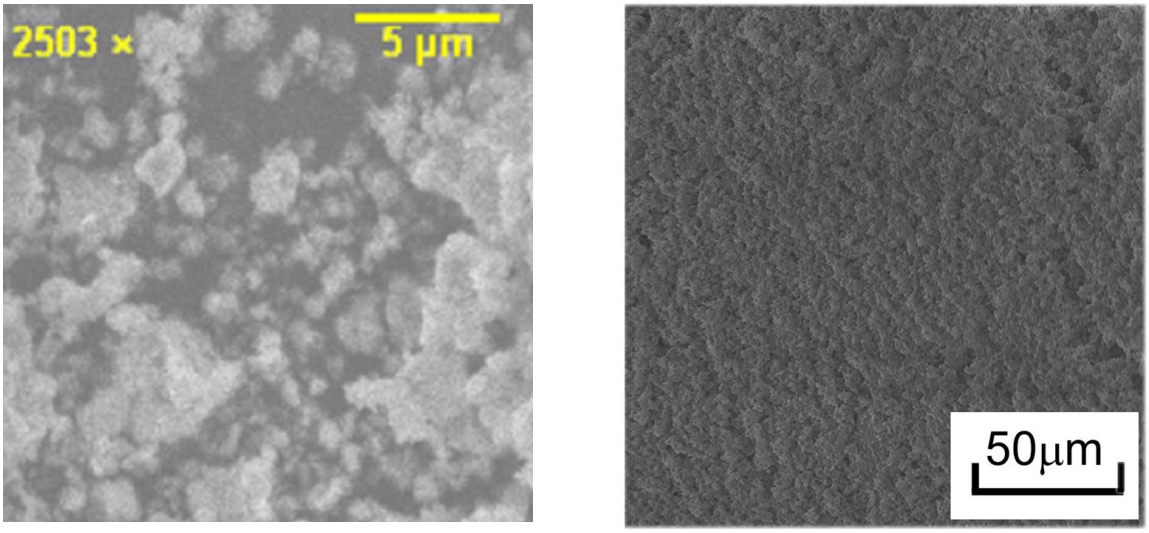

Figure 4.1.2-1. Appearance of Si_3N_4 powder

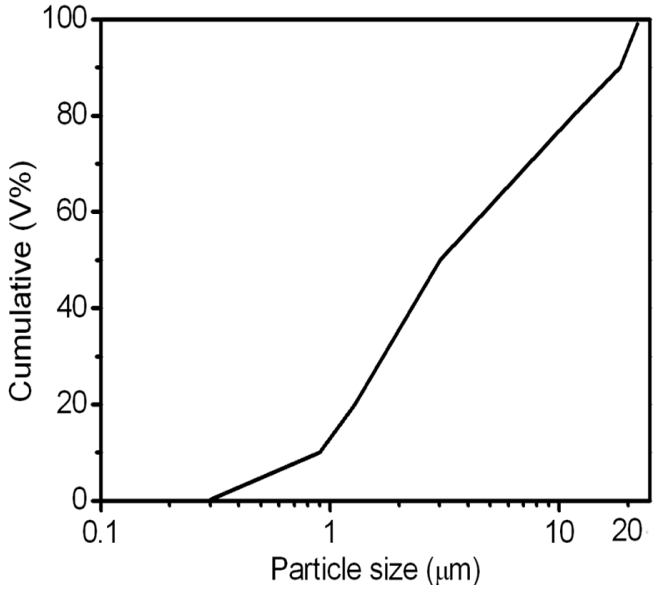

Figure 4.1.2-2 Size distribution of Si_3N_4 powder

4.2 MATERIAL FABRICATION PROCESS

4.2.1 3D PRINTING PROCESS

A 3DP system (Prometal R1, ExOne, USA), as shown in Fig. 4.2.1-1, was used to fabricate green samples.

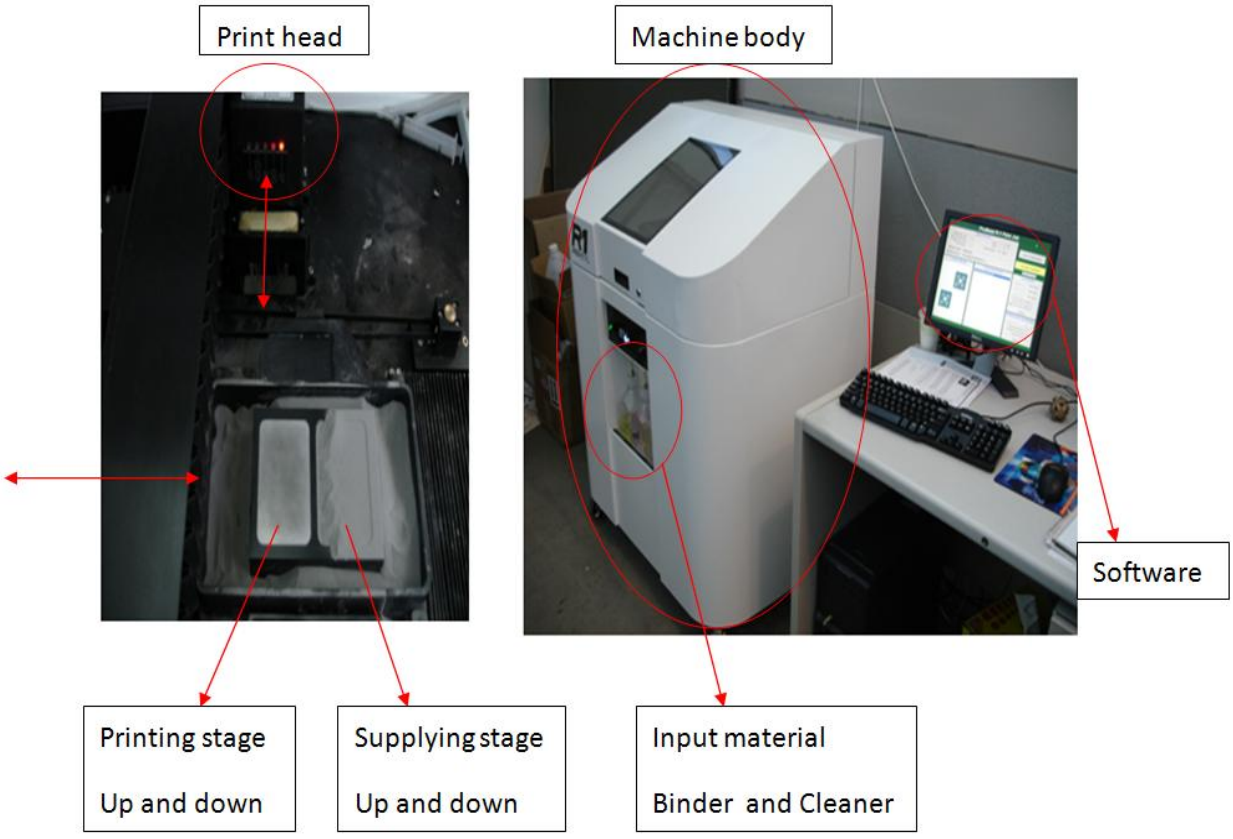

Figure 4.2.1-1. 3DP system (Prometal R1, Exone, USA)

The schematic illustration of the 3DP process is shown in Fig. 4.2.1.-2

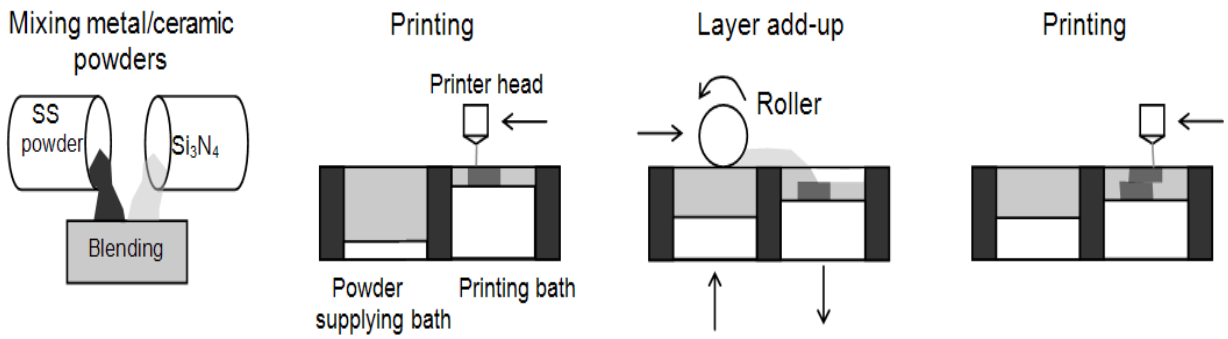

Figure 4.2.1-2. Schematic of 3DP procedures

1. 420 SS and Si_3N_4 powders were dry mixed and spread evenly over two adjacent beds, supply and print beds. Mixed powders with different Si_3N_4 wt% are shown in Fig. 4.2.1-3 and Fig. 4.2.1-4.

2. The two beds move up and down in contrast to each other in the vertical direction.

3. The supply bed begins at a lower level than the print bed to hold an abundant amount of powder necessary for printing.

4. An inkjet printer head then furnishes a binding fluid (PM-B-SR1-01, ExOne, USA) onto the powder over print bed at each separate layer.

5. Then, the supply bed goes upward in small intervals where the powder seems to slightly overflow the bed.

6. This overflow is then spread evenly from the supply bed to the print bed by a metallic roller to print the subsequent layer.

7. Repeating these steps, the powder builds upon itself to create a stable 3-D model.

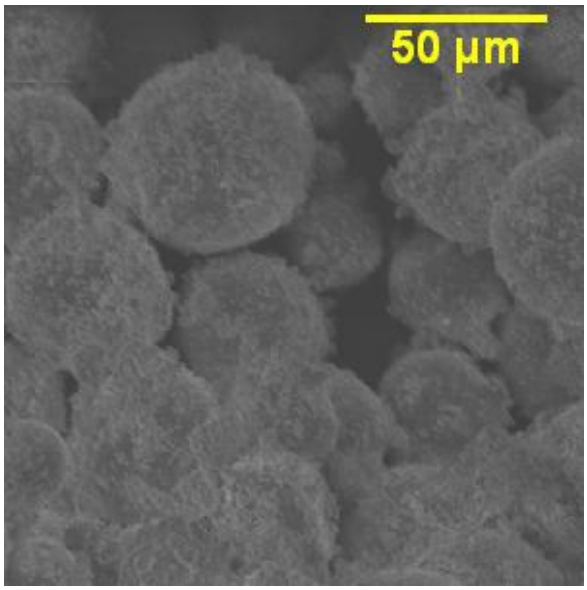

Figure 4.2.1-3. 420 SS powder mixed with 2.5wt% Si_3N_4

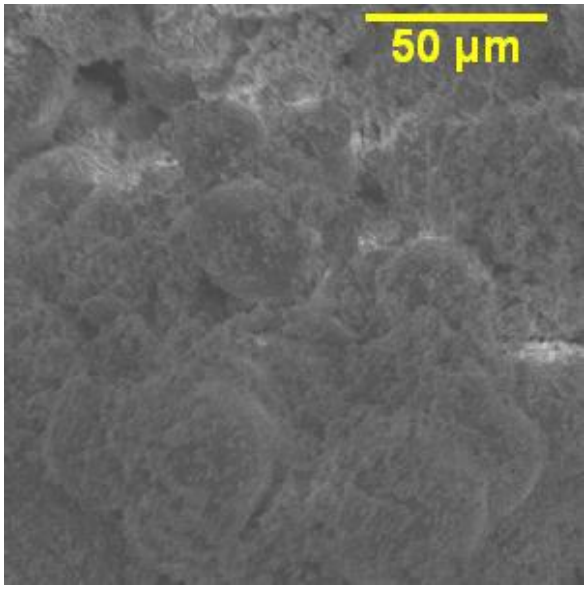

Figure 4.2.1-4. 420 SS powder mixed with 7.5wt% Si_3N_4

The green samples for the densification kinetics test are in a cube shape with edge length of 8 mm. The additional samples are prepared in an L shape with two arms whose lengths are 10

mm and 8 mm, representatively, for the dimension accuracy measurement. The green samples for Young's modulus test are rectangular parallelepipeds whose dimensions are 15.8 mm × 5.25 mm × 2.8 mm.

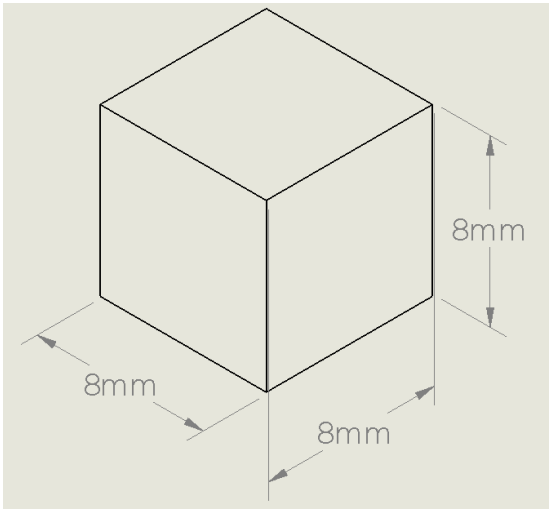

a)

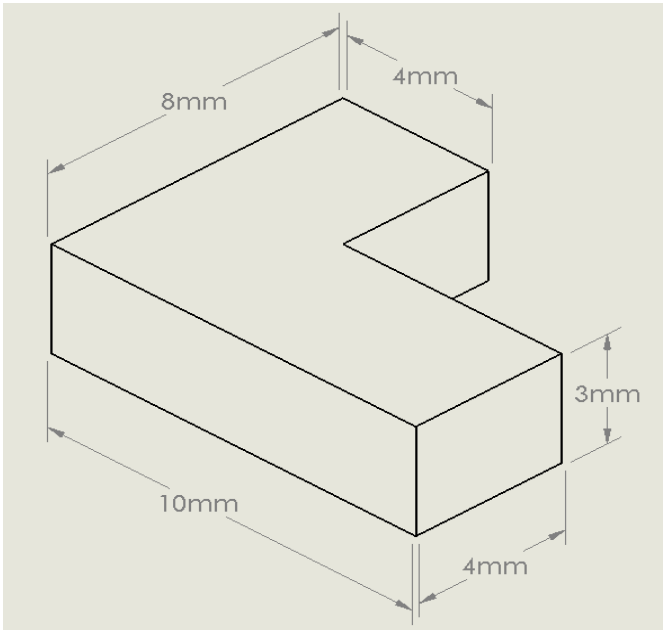

b)

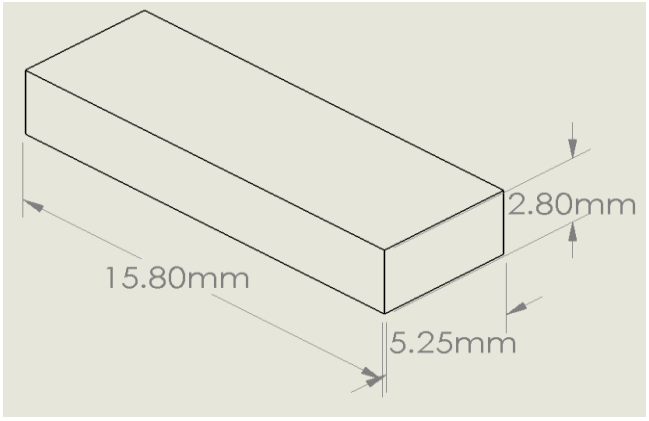

c)

Figure 4.2.1-5. Schematics of parts for a) densification study, b) dimensional accuracy test, and c) elastic modulus test.

4.2.2 POST PROCESS

After printing, the samples were cured in the furnace at 170ºC for 2 hours. The support powder then was removed using fine brushes and the green samples were ready for the sintering process. Several green samples were used to measure the green densities.

The real time sintering testing was performed using a Thermo-Mechanical Analyzer (TMA, Setaram 95, France) in the protective environment of argon gas. The ramp/soak profile is shown in Fig. 4.2.2-1. This sintering path was different from the one recommended by the manufacturer. However, as shown later, the temperature cycle used can achieve the samples with higher final relative densities. The pre-sintering (de-binding) was set at 240 ºC for 2 hours to remove cured polymeric binder material. Three final sintering temperatures: 1150, 1225, and 1300^{o}C, and three final soak durations: 2, 6, and 10 hours, were used to investigate the effect of sintering temperature and duration on the densification of the resulting samples. The ramp rate is 10^{o}C /min for both the heating and cooling cycles. The volume of each fully-sintered piece was also measured in water by Archimedes' principle.

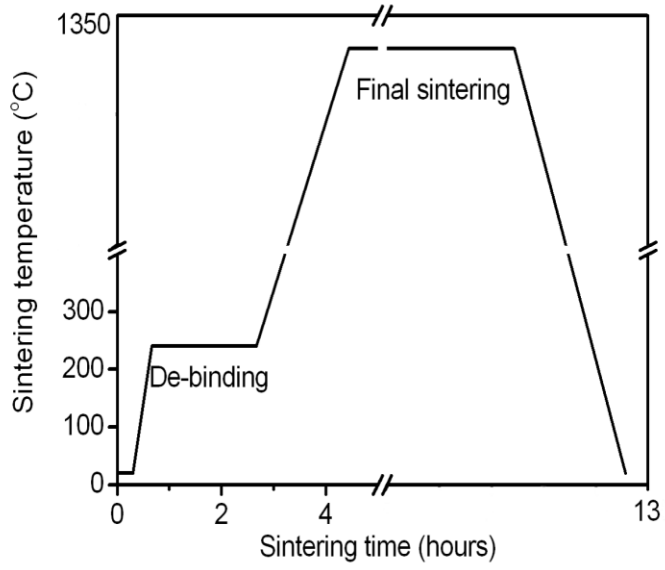

Figure 4.2.2-1. Ramp/soak profile for the sintering process.

Schematic of post process is shown in Fig. 4.2.2-2.

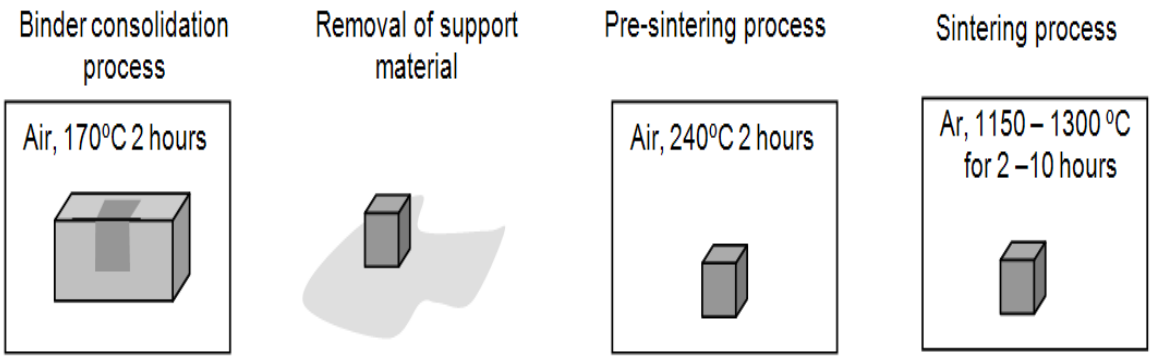

Figure 4.2.2-2. Schematic of 3DP post processes

Figure 4.2.2-3. Sintering furnace (Exone, USA)

4.3 EXPERIMENTAL DESIGN

4.3.1 DENSIFICATION STUDY

Three different process parameters are used for the densification study. Three input factors are sintering temperature, varied wt% of Si_3N_4, and sintering time. Other conditions than the input parameters, such as 3DP system set up shown in table 4.3.1-1, were consistent for all the experiments. The factors and levels chosen for the experiments matrix are shown in Table 4.3.1-2.

Table 4.3.1-1. 3DP system set up

3DP system parameters	Levels
Saturation %	35%
Drying time	20 sec
Drying power (0 to 100%)	65%
Layer thickness	100 μm

Table 4.3.1-2. Factors and levels chosen for the densification study

Process parameters	Levels
Sintering temperature	1150 ^{o}C, 1225 ^{o}C, 1300 ^{o}C
Wt% of Si_3N_4	0wt%, 2.5 wt%, 5 wt%, 7.5 wt%, 10 wt%, 12.5 wt%, 15 wt%
Sintering time	2hours, 6hours, 10hours

4.4 QUALITY ASSURANCE OF 3D PRINTED SAMPLES

4.4.1 DENSIFICATION

The degree of densification was determined by relative density. Relative density is expressed by the following equation.

$$Relative\ density = \left[\frac{Measured\ density}{Ideal\ density}\right] \times 100 \qquad \text{(Eq. 4.4.1-1)}$$

The measured density of each sample was calculated based on the volume by Archimedes' principle and corresponding sample mass. Ideal density is calculated based on the assumption that there is no void in the sintered sample, and can be expressed by following equation.

$$Ideal\ Density = \{(Density\ of\ 420SS) \times (wt\%\ of\ 420SS)\} + \{(Density\ of\ Si_3N_4) \times (wt\%\ of\ Si_3N_4)\}$$

(Eq. 4.4.1-2)

The density values used were 7.75 and 3.44 g/cc for 420 SS and Si_3N_4, respectively [50].

4.4.2 MICROSTRUCTURE OBSERVATION

A Scanning Electron Microscope (PSEM-75, ASPEX Instrument, USA) analysis was performed to study the microstructures of 3DP processed metal parts. In addition, in order to verify the components of the samples, Energy-Dispersive X-ray spectroscopy (EDX) analysis was performed.

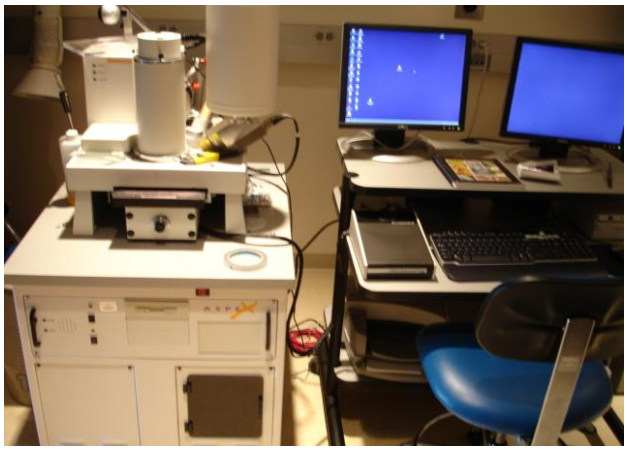

Figure 4.4.2-1. Scanning Electron Microscope with EDX capability (Aspex, USA).

4.4.3 DIMENSIONAL ACCURACY

The dimensional accuracy of each sintered sample was measured using a measuring microscope which has an optical microscope function with a 3-axis digital readout capability in 0.0005 mm resolution (Metronics, USA) as shown in Fig. 4.3-1. While focusing onto the contour of samples, the coordinates of contour can be obtained at the same time since the coordinates of focused points are shown on 3-axis digital readout automatically. Based on the coordinates obtained, discussions for the dimensional accuracy were made such as shape maintenance ability and shrinkage behaviors.

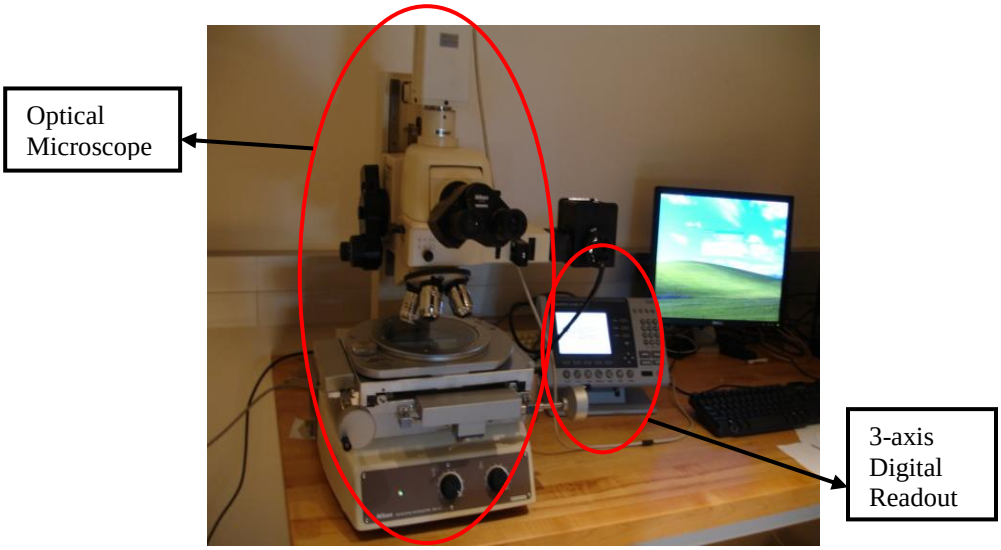

Figure 4.4.3-1. Measuring microscope (MM-40, Nikon, Japan) with 3-axis digital readout (Metronics, USA)

4.4.4 MECHANICAL PROPERTIES TESTING

The three-point bending method was used for measuring Young's modulus of materials. The Knoop microhardness test was performed by DM-400(Leco, Japan) as shown in Fig. 4.4.4-1. All samples were polished before the testing. In order to obtain average microhardness value throughout the samples, 5 measurements were taken along the y-axis at intervals of 1mm for each sample. Indentation load of 100g and time of 18 second were used for the testing.

Figure 4.4.4-1. Microhardness tester (Leco, Japan).

CHAPTER FIVE

RESULTS AND DISCUSSION

5.1 DENSIFICATION STUDIES

5.1.1 MICROSTRUCTURES AND COMPONENTS OF GREEN SAMPLES

After the curing process, the microstructures of various green samples with different Si_3N_4 proportions were observed. For the green samples without Si_3N_4 as shown in Fig. 5.1.1-1, the 420 SS powders have clear boundaries, which are attached by the solid binder material.

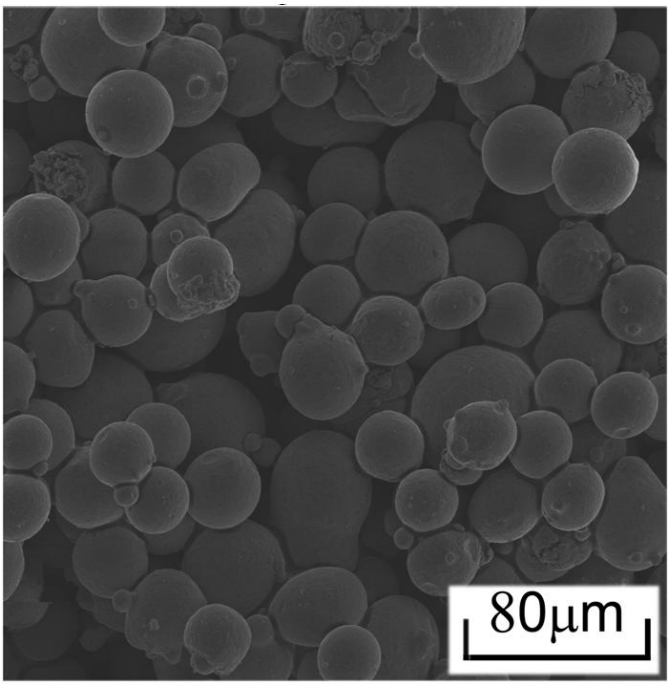

Figure 5.1.1-1. Micrograph of a green part with 0 wt% Si_3N_4

With Si_3N_4 added into the powder system, the interstitial space among 420 SS powders was filled in by smaller Si_3N_4 powders. Also due to the smaller particle size of Si_3N_4 compared to 420 SS powder, the powder system with the addition of Si_3N_4 powder has a much larger specific surface area than that of pure 420 SS powder, resulting in more binder phase in the powder. Fig. 5.1.1-2 shows that most of Si_3N_4 powders are mixed with the binder phase and in the boundaries of 420 SS powders. These two factors result in the 420 SS powders "dispersing" into the mixture of Si_3N_4 and binder. The 420 SS powders form dumbbell or more complex "agglomerates." Voids are prevalent in the green samples.

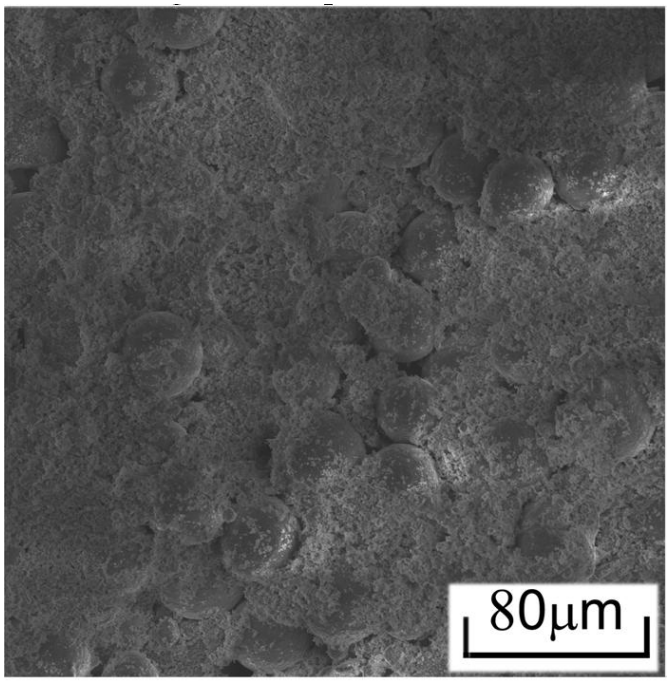

Figure 5.1.1-2. Micrograph of a green part with 12.5 wt% Si_3N_4

In order to verify the compositions of the green parts, the rules of mixture was used to calculate volume % of each phase of the green parts. The volume % of 420 SS, Si_3N_4, binder, and void content can be found by the following equations:

$$Vol\,\%\,(420\,SS) = \left[\frac{\left(\frac{Weight(420\,SS)}{Density(420\,SS)}\right)}{Volume(Total)}\right] \times 100 \qquad \text{(Eq. 5.1.1-1)}$$

$$Vol\,\%\,(Si_3N_4) = \left[\frac{\left(\frac{Weight(Si_3N_4)}{Density(Si_3N_4)}\right)}{Volume(Total)}\right] \times 100 \qquad \text{(Eq. 5.1.1-2)}$$

$$Vol\,\%\,(Binder) = \left[\frac{\left(\frac{Weight(Binder)}{Density(Binder)}\right)}{Volume(Total)}\right] \times 100 \qquad \text{(Eq. 5.1.1-3)}$$

$$Vol\,\%\,(Void) = \left[1 - \frac{\left(\frac{Weight(SS\,420)}{Density(SS\,420)}\right) + \left(\frac{Weight(Si_3N_4)}{Density(Si_3N_4)}\right) + \left(\frac{Weight(Binder)}{Density(Binder)}\right)}{Volume(Total)}\right] \times 100$$

(Eq. 5.1.1-4)

Weights of 420 SS and Si_3N_4 are calculated based on wt% of each component in sintered samples, assuming the sintered samples consist of only 420 SS and Si_3N_4. Weight of binder was obtained from the mass change of a green sample and a sintered sample. The density values used were 7.75 g/cc for 420 SS and 3.44 g/cc for Si_3N_4 [50], and the density of binder used was 1.05g/cc which is obtained from the manufacturer. Table 5.1.1-1 is the volume % values for each component for samples with various Si_3N_4 contents obtained from the rule of mixture method, and Fig. 5.1.1-3 is the plot of the values in Table 5.1.1-1.

Table 5.1.1-1. Volume % of each component of different green samples.

Si_3N_4 wt%	Volume % on the green parts			
	SS powder	Si_3N_4 powder	Binder material	Void
0	52.2±0.1	0±0	3.9±0.1	43.9±0.1
2.5	49.1±0.3	2.8±0.1	7.5±0.1	40.6±0.3
5	48.2±1.4	5.6±0.2	10.9±0.3	35.4±1.8
7.5	46.0±0.3	8.3±0.1	15.7±0.1	30.1±0.3
10	40.0±0.1	9.9±0.1	14.1±0.1	36.0±0.1
12.5	36.6±0.1	11.6±0.1	16.3±0.1	35.4±0.1
15	34.5±0.1	13.5±0.1	18.5±0.1	33.4±0.2

As shown in Fig. 5.1.1-3, the content of the binder material increases while the content of 420 SS powder and void decrease when Si_3N_4 wt% increases. As explained above, the powder mixture with a higher Si_3N_4 content has a larger specific surface area, which results in more liquid binder phase attached in the printing process. Consequentially, the void and 420 SS powder content decrease.

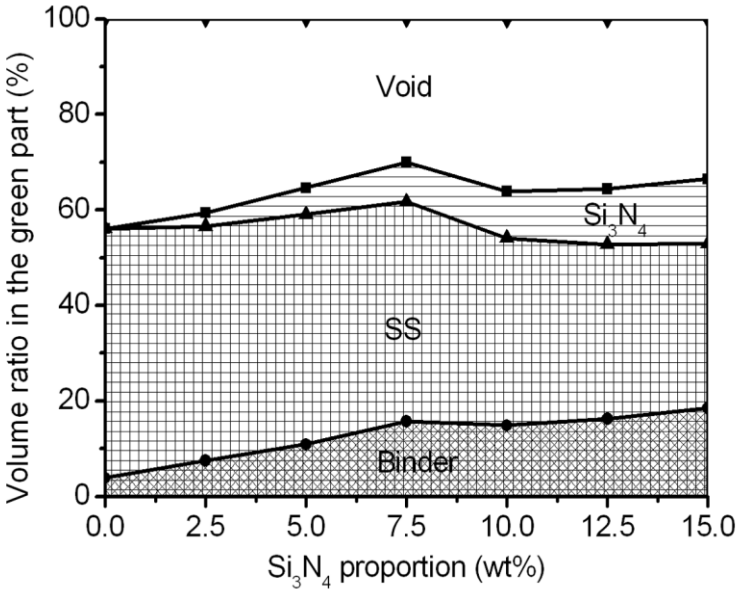

Figure 5.1.1-3. Volume ratio of each component in various green parts.

5.1.2 SINTERING KINETICS OF 420 SS-SI_3N_4 ALLOY

Fig. 5.1.2-1 shows the sintering kinetics curves of representative samples. All the curves share three common characteristics.

1) Before sintering starts, due to thermal expansion effect in response to heating, the trend of curves increases in the initial plateau.

2) However, there are three valleys in the pre-sintering part, which fall into the temperature ranges of 205 to 240^{o}C, and 732 to 880^{o}C. The first valley is a result of decomposition and vaporization of binder material. The second valley is related to the heating rate jumping from 0 to 10°C /min after the 2-hour iso-thermal stage at 240°C. The third valley is due to the Austenizing phase transition. Austenizing begins for the 420 SS at 727^{o}C and completes around 850^{o}C [51]. When the furnace temperature reaches at 732^{o}C, the phase transition from BCC to FCC begins, resulting in the sudden shrinkage in the third valley.

3) The sintering begins around 1100^{o}C (3.83 hours); large shrinkage was found in the sintering step.

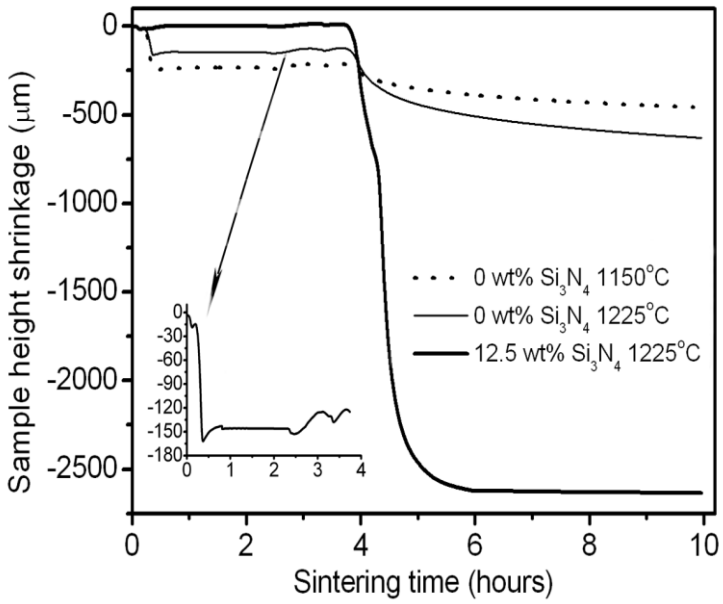

Figure 5.1.2-1. The temperature dependent sintering kinetics curves for the representative samples. The small figure shows the pre-sintering curve of 0wt% Si_3N_4 sample sintered at 1225°C. (The soak duration is 6 hours for all three curves).

There are, however, the important differences among the densification kinetics curves.

1) If one approximates the pre-sintering parts in Fig 5.1.2-1 to linear line, the line for the sample with 12.5wt% Si_3N_4 changes less drastically as a function of time than that for the sample with 0wt% Si_3N_4. This is due to the lower thermal expansion coefficient of Si_3N_4 ($3.1\times10^{-6}m^2/K$ [50]) compared that of stainless steels (10.26×10^{-6} m^2/K [50]).

2) For the sample with 12.5 wt% Si_3N_4, the sample height change almost converges after 4-hour soak in Fig 5.1.2-1, which represents that the sintering process has matured. All the samples with higher than 5wt% Si_3N_4 share this characteristic with final sintering temperature at 1225 or 1300^{o}C. For other samples, the shrinkage curve changes more drastically even after 6 hour soak, which means the sample is still far from full-sintering. However, extending final soak duration hardly affects the final shrinkage value, Δh. For example, the shrinkage of the samples with 0 wt% Si_3N_4 sintered at 1225^{o}C with 10-hour soak duration was increased only 4.1% comparing to that with 2-hour soak duration. The soak duration was the least influential factor for the dimensions change among the three input factors, the content of Si_3N_4, sintering temperature and sintering duration. Therefore, only experimental results by 6-hour soak duration will be discussed below.

3) The dimensional change was affected enormously by temperature variation and Si_3N_4 proportion. If the dimensional shrinkage ratio in vertical direction (to be called the height shrinkage ratio) $h\%$ is defined as $h\%=\Delta h/h_{green}$, where h_{green} is the height of the green sample, the dependence of $h\%$ on the proportion of Si_3N_4 and final sintering temperature is shown in Fig 5.1.2-2. The height shrinkage ratio continuously increases as the final sintering temperature increases for the samples with the same components. The driving force of pore shrinkage and surface transport increases as sintering temperature increases, resulting in a higher dimensional shrinkage [52,53]. Below 12.5 wt% Si_3N_4, the height shrinkage ratio increases as the proportion

of Si_3N_4 increases. This is due to the enhanced atomic transport/material diffusion of 420 SS with the addition of Si_3N_4. However, even 1300ºC is still much lower than the fully sintering temperature of Si_3N_4 powders [54]. Therefore, once the proportion of Si_3N_4 is higher than the threshold value of 12.5 wt% of Si_3N_4, , the sintering kinetic begins to decrease, resulting in less shrinkage ratio as shown in Fig 5.1.2-2.

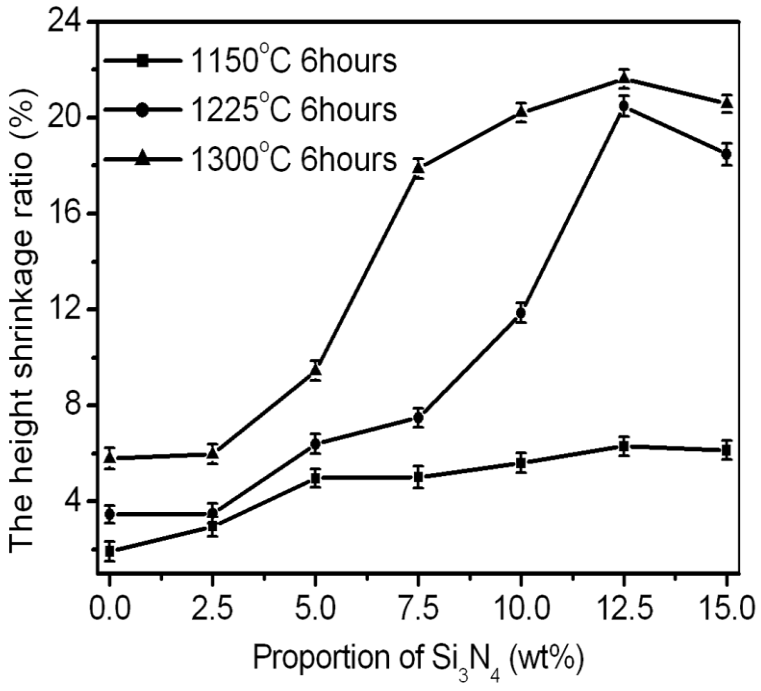

Figure 5.1.2-2. The dependence of height shrinkage ratio on the proportion of Si_3N_4 and sintering temperature.

During the sintering, as well as the shrinkage in the vertical direction (the height), the dimensions in all three directions were also shrunk. For the cubic samples, the shrinkage ratios along any edges are almost similar to one another. That is, the trend of the sintering process for the cubic samples is a self-similar (isotropic) one. Therefore, the dependence of volume shrinkage ratio *V%*, which is defined as $V\%=1-(V_{sintered}/V_{green})$, on the proportion of Si_3N_4 and the final sintering temperature is similar to Fig. 5.1.2-3 [51].

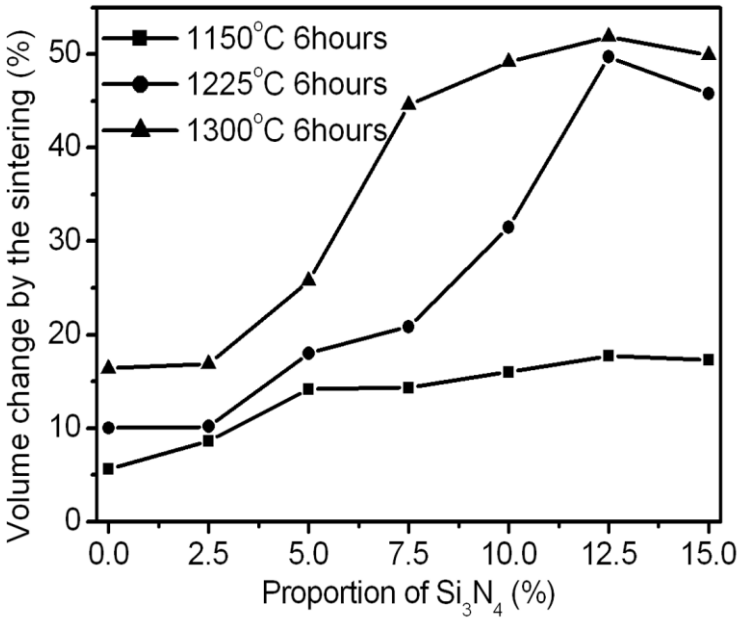

Figure 5.1.2-3. The dependence of volume shrinkage on the proportion of Si_3N_4 and sintering temperature [51].

5.1.3 DENSIFICATION OF 420 SS-SI_3N_4 ALLOYS BY SINTERING

Due to the decomposition and vaporization of the binder phase, mass loss is always inevitable in the sintering of the 3DP processed 420 SS samples. The mass change is independent of the final sintering temperature since all binder materials have vaporized out of the samples as shown in Fig. 5.3-x. However, the mass loss was near-linear starting from $1.01 \pm 0.002\%$ to $5.84 \pm 0.021\%$ as the content of Si_3N_4 powder increases from 0 wt% to 15 wt% since the powder mixture with more Si_3N_4 attached more liquid binder during the printing process (Fig. 5.1.3-1).

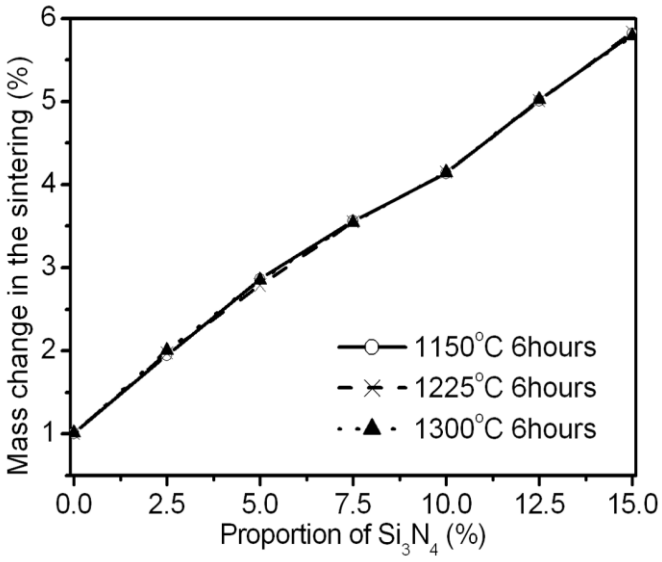

Figure 5.1.3-1. The dependence of mass change by the sintering on the proportion of Si_3N_4 and sintering temperature.

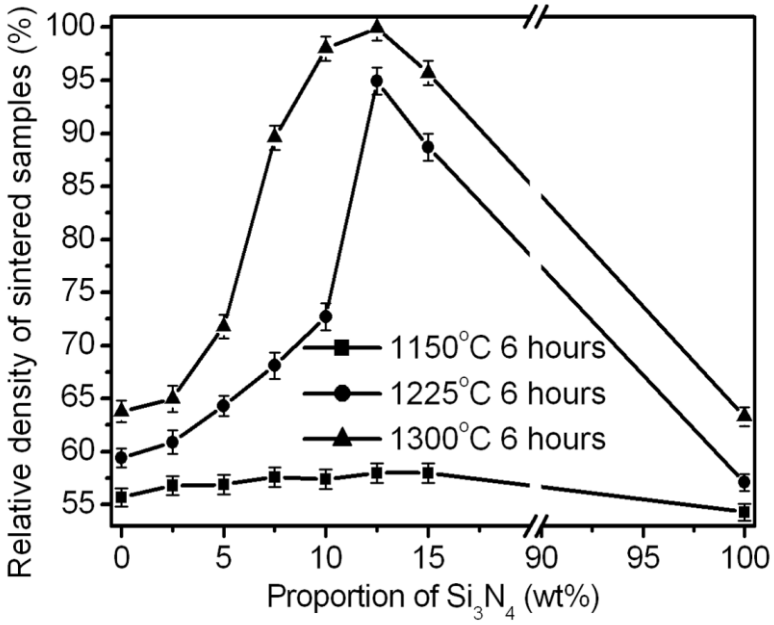

Figure 5.1.3-2. The dependence of relative densities of the sintered samples with varied proportions of Si_3N_4 and sintering temperature (Values of pure Si_3N_4 were acquired from sintered cold pressed samples under 80MPa).

Fig. 5.1.3-2 shows the relative density data for the various samples. The relative densities of the samples sintered at 1150ºC are around 57%. At 1150°C, 420 SS is only at the initial stage of sintering [55] and Si_3N_4 does not even begin to sinter [54]. Therefore, only decomposition of the binder phase, not sintering of SS and Si3N4 powder mixtures, mainly causes the densification of the samples sintered at 1150ºC, resulting in relatively low final density values. Samples sintered at 1225 and 1300ºC feature much higher final densities. The relative density increases with the increase of the Si_3N_4 contents till the content of Si_3N_4 reaches 12.5 wt%. Beyond 12.5 wt%, the final relative densities have decreased. This characteristic is the same as the height shrinkage ratio-Si_3N_4 proportion relationship in Fig. 5.1.2-1. The highest relative density of 99.8% is obtained for the sample with 12.5 wt% Si_3N_4 sintered at 1300ºC. The relative densities

dramatically increase from 7.5 to 12.5 wt% Si_3N_4 when the samples sintered at 1225ºC and from 5 to 10 wt% Si_3N_4 when sintered at 1300ºC. The Si-Fe phase diagram [56], as shown in Fig. 5.1.3-3, shows that liquid phase can be produced above 1225ºC (1498K) once the silicon is beyond 0.15 mole fraction (Si wt% is higher than 6.9 wt%). As the silicon content increases, the liquidation-beginning temperature is lower.

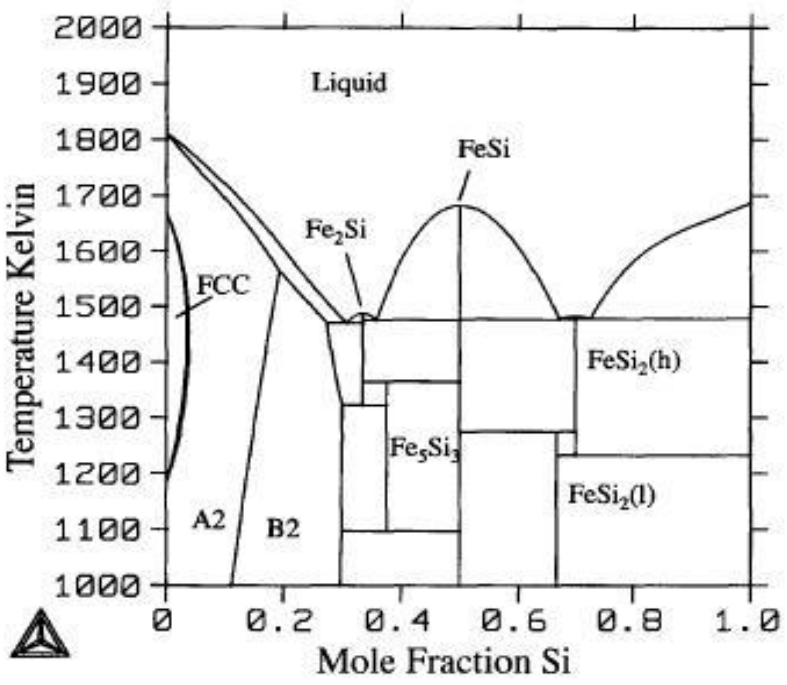

Figure 5.1.3-3. The Si-Fe phase diagram [56]

The liquid phase induces transient liquid phase sintering, which offers faster diffusion of alloying elements and accelerates the densification [57]. Therefore, the dramatic increase of the final density was observed in the two process windows; between 7.5 and 12.5 wt% Si_3N_4 when the samples sintered at 1225ºC, and between 5 and 10 wt% Si_3N_4 when sintered at 1300ºC mentioned above. And the latter process window has a lower content boundary for Si_3N_4 than the former process window. A similar trend in Fig. 5.1.3-2 has been reported by Farid et al. [58] that 465 stainless steel with addition of only 5wt% Si_3N_4 reaches the highest relative density (98.5% at 1300ºC for 1 hour). The discrepancy between the present report and that of Farid et al. [58] may be due to the difference in the type of stainless steel and green density. Due to the high nickel content (10.7 wt%) in 465 SS, the bonding between nickel and Si_3N_4 forms very easily once the temperature becomes higher than 850°C despite of its low proportion of the Si_3N_4 powder [54,59]. This binding can enhance the diffusion of Si into the steel and then accelerate densification. Because 420 SS has only 0.47 wt% of nickel on the material system, much more Si_3N_4 (7.5wt% to 12.5wt%) is required to accelerate densification.

5.1.4 MICROSTRUCTURES OF SINTERED SAMPLES

In the sintering process, due to solid-state atomic transport phenomenon and/or liquid phase formation, bonds between particles form. The bonds cause the increase in the average size of particles (coarsening) as well as the elimination of solid/vapor interfaces and grain growth (densification) [52,53,66]. Therefore, the microstructures change during the sintering process. Coble [55] proposed three stages of sintering:

1) The initial stage: the inter-particle contact area increases by neck growth, with relative density increases to 60-75%

2) The intermediate stage: Continuous pore channels are seen at the triple points (three-grain junctions) and relative density increases up to 90%.

3) The final stage: Pore phase is eventually pinched off. Continuous pore channels disappear. Individual pores are either lenticular on grain boundaries, or rounded within a grain.

Fig. 5.1.4-1, Fig. 5.1.4-2, and Fig. 5.1.4-3 shows the micrographs of representative 420 SS-Si_3N_4 MMCs sintered at various temperatures. Under 1150^oC sintering, most 420 SS grains are still in the original ball shape. However, necks among grains were observed. . All pores are interconnected. These microstructural characteristics reveal sintering occurred but only in the initial stage. As the proportion of Si_3N_4 increases, the dumbbell shape grains increase. Also, once the Si_3N_4 proportion is higher than 10 wt%, the surface coarsening begins as shown in Fig. 5.1.4-1, c). These phenomena show that the increased Si_3N_4 proportion enhances atomic transport of 420 SS.

At 1225 and 1300^oC, samples with varied Si_3N_4 wt% show different microstructures. If the wt% of Si_3N_4 is less than or equal to 2.5%, the microstructures are still similar to those sintered at 1150^oC. The sintering is only in the initial stage. However, for other samples with higher Si_3N_4 proportion, the initial ball shape of green particles has been totally destroyed to a solid skeleton structure [52] and almost all pores are isolated, which means the high addition of Si_3N_4 not only enhances the atomic transport/material diffusion also accelerates the sintering into medium stage.

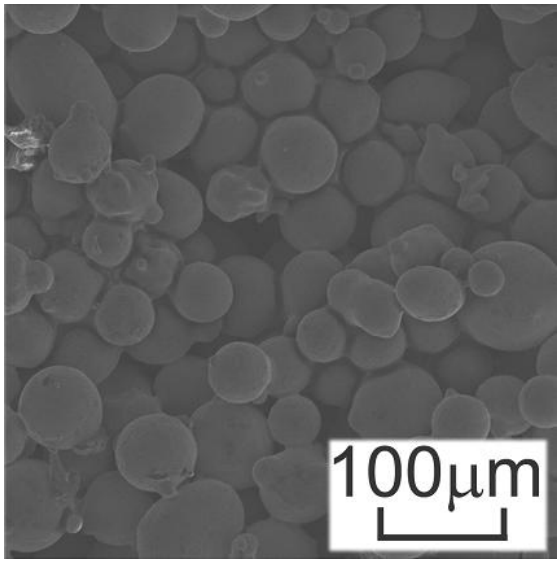

a)

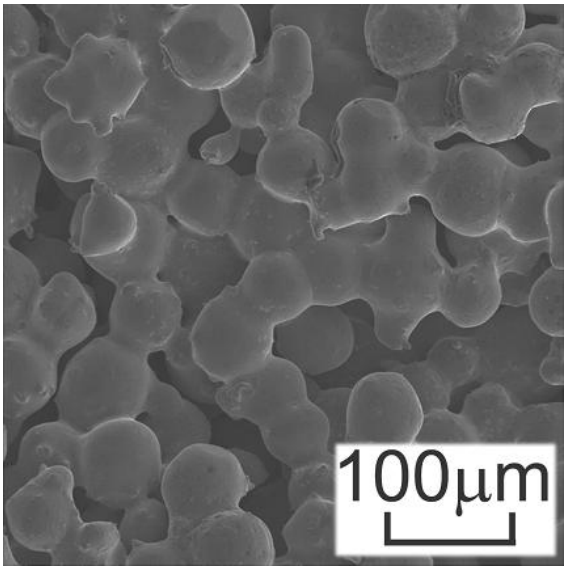

b)

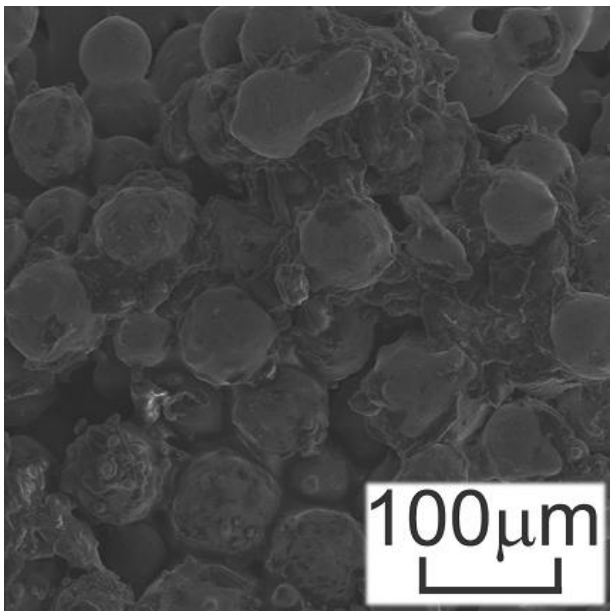

c)

Figure 5.1.4-1. Micrographs of sintered parts of a) 0 wt% Si_3N_4 sintered at 1150 ^oC, b) 7.5 wt% Si_3N_4 sintered at 1150 ^oC, c) 12.5 wt% Si_3N_4 sintered at 1150 ^oC for 6hours

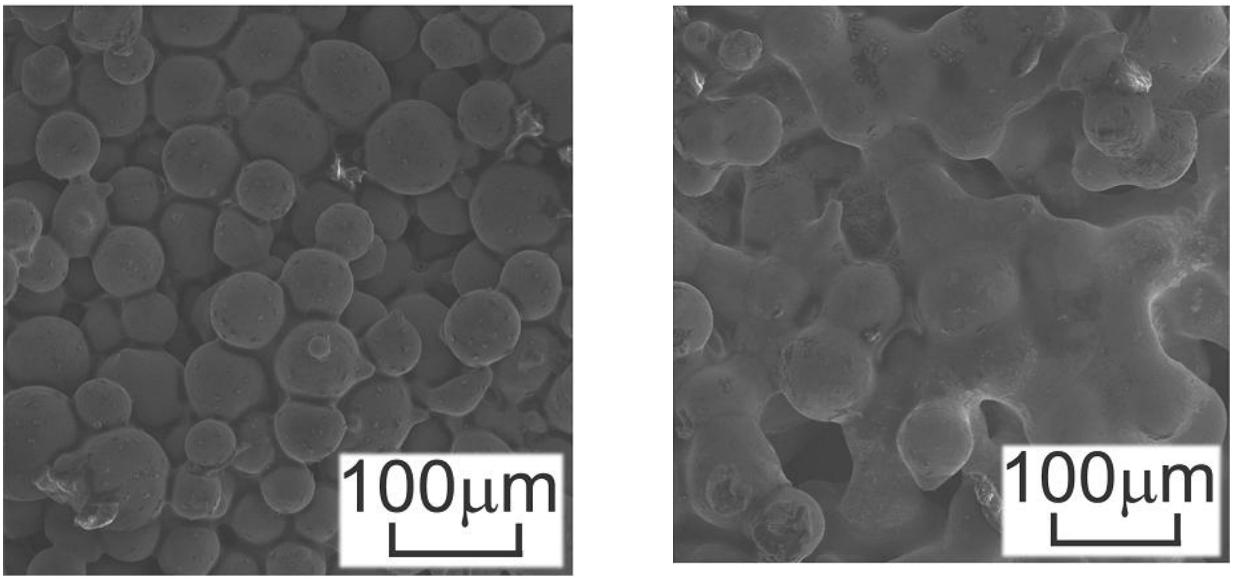

a) b)

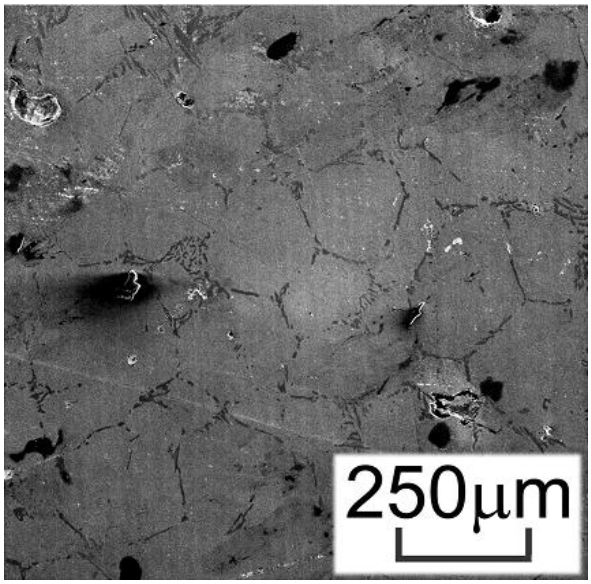

c)

Figure 5.1.4-2. Micrographs of sintered parts of a) 0 wt% Si_3N_4 sintered at 1225 ^oC, b) 7.5 wt% Si_3N_4 sintered at 1225 ^oC, c) 12.5 wt% Si_3N_4 sintered at 1225 ^oC for 6hours

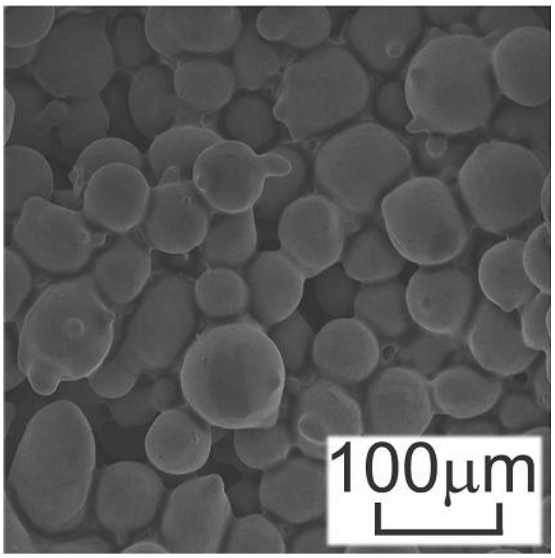

a)

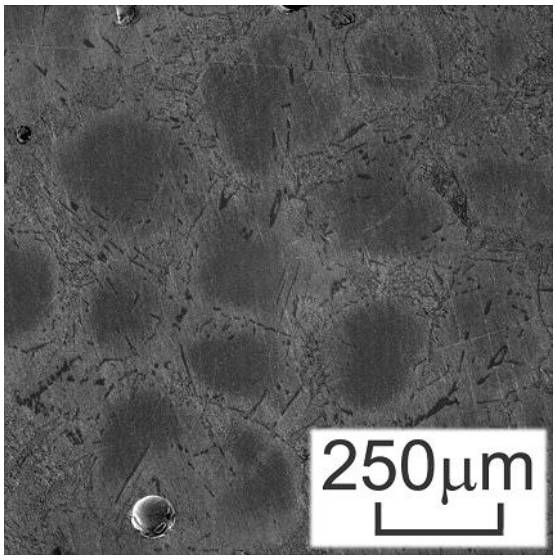

b)

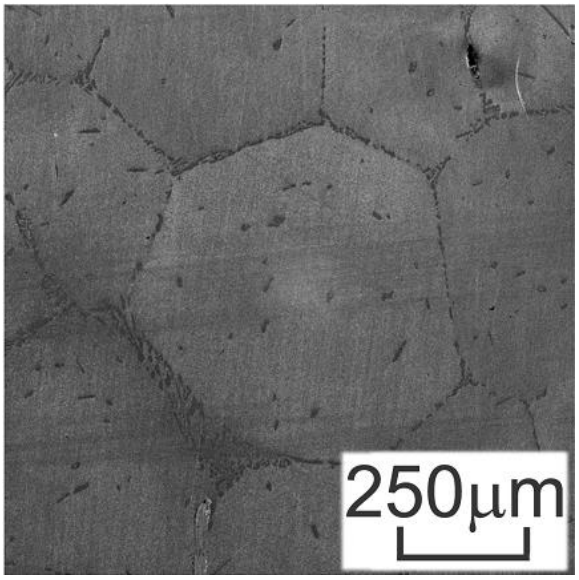

c)

Figure 5.1.4-3. Micrographs of sintered parts of a) 0 wt% Si_3N_4 sintered at 1300 ^oC, b) 7.5 wt% Si_3N_4 sintered at 1300 ^oC, c) 12.5 wt% Si_3N_4 sintered at 1300 ^oC for 6hours

If focused on the boundaries of the 420 SS grains for the Si_3N_4-420 SS sintered samples, the reinforced Si_3N_4 grains can be observed, as shown in Fig. 5.1.4-4. The size of those Si_3N_4 particles is still around 2um. We also dissolved several samples sintered at 1300^{o}C by 25% of HCl + H_2SO_4 solution. After full reaction, some black particles left in the bottom of the bottle. The particle size distribution of those black particles was in a similar profile of Fig. 4.1.2-2, and the EDS analysis indicated that they are Si_3N_4. The mass ratio of those "deposit" is about 1.3 ± 0.2 wt% of the original green samples with 5 wt% Si_3N_4, and 5.9 ± 0.4 wt% of those with 10 wt% Si_3N_4. From these results, it is reasonable to consider that up to 4wt% Si_3N_4 are dissolved into the 420 SS during the sintering process.

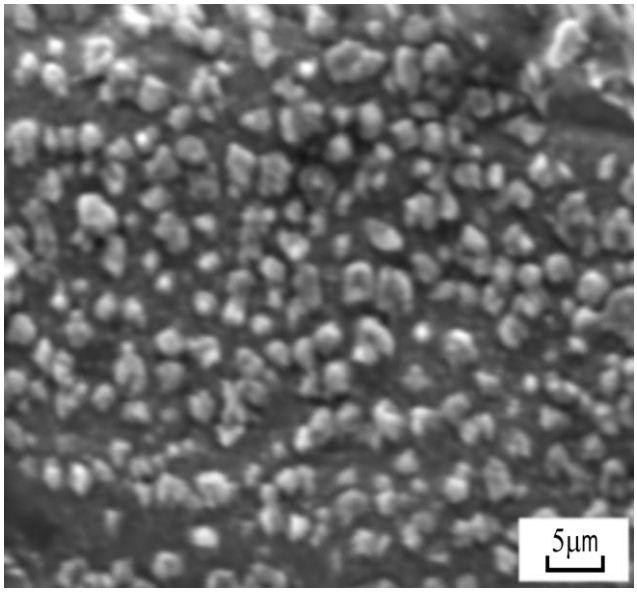

Figure 5.1.4-4. The reinforced Si_3N_4 particles in the boundaries of 420 SS grain of sample with 7.5% Si3N4 sintered at 1300^{o}C for 6 hours.

Fig. 5.1.4-5, Fig. 5.1.4-6, and Fig. 5.1.4-7 show the micrographs of the representative sintered 420 SS/Si_3N_4 samples and their energy dispersive X-ray (EDX) analysis results. Comparing the grain size of the samples, the grain size increases with the increase of the Si_3N_4 proportion when the sintering temperature is the same. Also, the grain size increases as the sintering temperature increases for the samples with the same Si_3N_4 proportion. It is observed from Fig. 5.1.4-5 that the grain size is around 40 to 50μm, similar to the size of green 420 SS powder. There is no obvious grain growth. All samples sintered at 1150^oC and samples with 0-5 wt% Si_3N_4 sintered at 1225 and 1300^oC (Sample Group A) shared these microstructural characteristics. The sintering of these samples is only in the initial stage. The sintering kinetics are dominated by either solid atomic transport or transient liquid phase sintering, resulting in less than 70% relative densities in Fig. 5.1.3-2 for these samples. Fig. 5.1.4-6 and 5.1.4-7, however, exhibit obvious grain growth. The grain sizes become around 150μm and 350μm respectively. In the sintering of these samples, liquid phase formed, which causes the elimination of solid/vapor interfaces and grain growth, resulting in much higher relative densities. The sintering is in the intermediate or final stage. Samples with over 7.5 wt% Si_3N_4 sintered at 1225 and 1300^oC shared these sintering characteristics (Sample Group B).

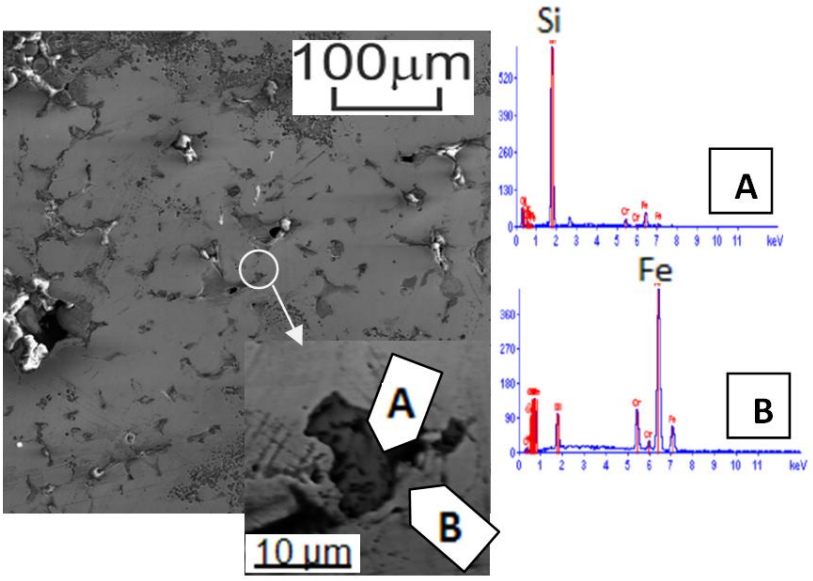

Figure 5.1.4-5. The micrograph of etched sample of 420 SS with Si_3N_4 of 7.5wt% sintered at 1225 ^{o}C and EDX analysis results(Etchant composition: HCl of 5ml, Ethanol of 95ml, Picric acid of 1g)

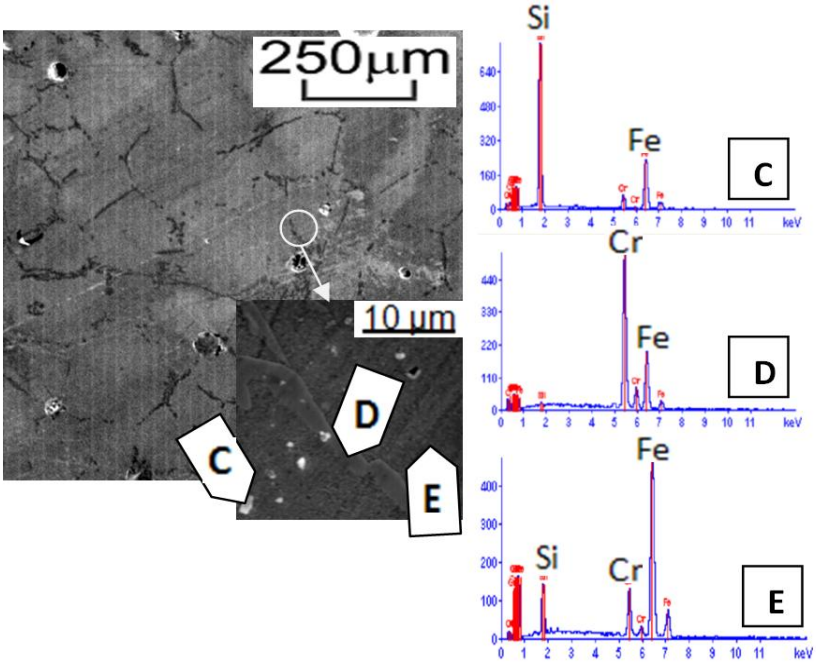

Figure 5.1.4-6. The micrograph of etched sample of 420 SS with Si_3N_4 of 12.5wt% sintered at 1225 ^{o}C and EDX analysis results(Etchant composition: HCl of 5ml, Ethanol of 95ml, Picric acid of 1g)

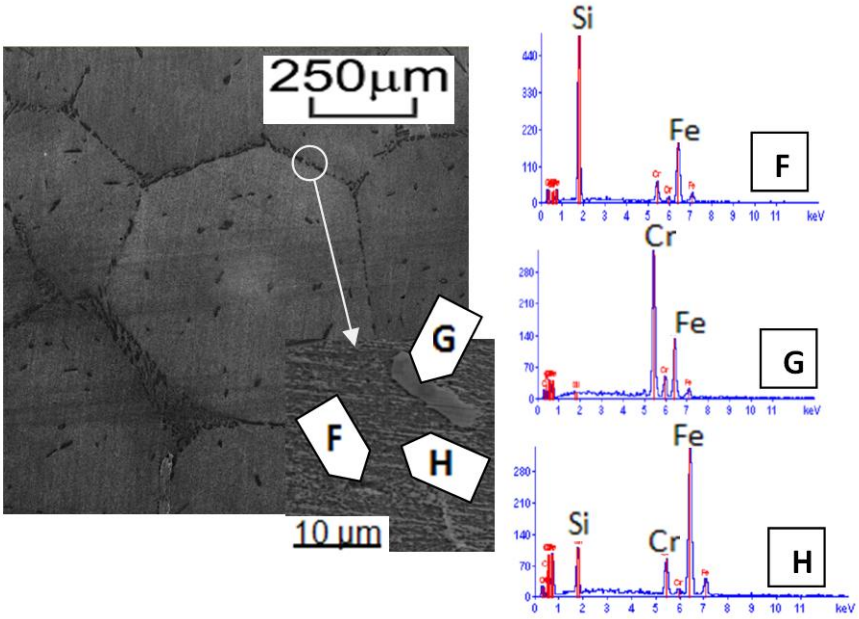

Figure 5.1.4-7. The micrograph of etched sample of 420 SS with Si_3N_4 of 12.5wt% sintered at 1300 ^oC and EDX analysis results(Etchant composition: HCl of 5ml, Ethanol of 95ml, Picric acid of 1g)

The EDX analysis results on the grain boundaries for the samples in Sample Group B show the precipitates of chromium and ferrous compounds. Such precipitates do not exist for Sample Group A. The precipitates are speculated as $M_{23}C_6$ type carbides, $Cr_{23}C_6$ (M stands for metal elements). $M_{23}C_6$ carbides are often observed in the intergranular positions after solution treatment and aging in most austenitic stainless steels [60]. According to Tarasenko [61], $M_{23}C_6$ precipitates could be formed in martensite steel, whose contents are almost identical to SS 420. The $M_{23}C_6$ carbide containing $Cr_{23}C_6$ of around 65% and $Fe_{23}C_6$ of 20% was precipitated in the grain boundaries of the martensite steel after heat treatment [61]. Therefore, it can be speculated that the precipitates that were formed in grain boundaries for Sample Group B are mostly $M_{23}C_6$.

5.2 DIMENSIONAL ACCURACY

5.2.1 DIMENSIONS PARALLEL TO THE BUILD PLATFORM

In order to quantify dimensional change for the 3DP parts, the L shape samples were printed with various Si_3N_4 contents and sintering temperature. For the L shape samples, the "L" shape was printed parallel to the build platform (X and Y directions). Length of 6 edges at the horizontal top surface for the samples was measured using the optical microscope with 3-axis digital readout capability in 0.0005 mm resolution (Metronics, USA). Because the dimensions parallel to the build platform are measured, there is negligible gravity effect on the dimensional change [62]. Average dimensional change from the nominal dimensions (i.e. the CAD dimensions) in percentage is shown in Fig. 5.2.1-1. It can be clearly seen that all dimensions in the green state are about 1% greater than nominal with a slight trend for the samples with higher Si_3N_4 contents to be more undersized. In addition, dimensional errors (standard deviations) in shrinkage are decreasing with increasing Si_3N_4 wt% for the green samples. This is due to finer Si_3N_4 powders locate gaps among SS 420 powders to stabilize the shape of the green samples. For sintered samples at the sintering temperature of 1150ºC, average shrinkage % ranges from –3 % to –5 % no matter how much Si_3N_4 wt% is included in the material system. However, average shrinkage % from the nominal dimensions decreases with increasing Si_3N_4 wt% when the samples are sintered at 1225ºC and 1300ºC. Average shrinkage of 21% is achieved for the sample with 12.5 wt% Si_3N_4 sintered at 1225ºC. This high shrinkage can possibly attributed to the effects of transient liquid phase sintering occurred at the sample sintered at 1225ºC and 1300ºC. As the samples contain 10 wt% to 15 wt% Si_3N_4, the severe distortion is found after sintering at 1300ºC. Note that standard deviation or errors in dimensional shrinkage for the samples containing various Si_3N_4 wt% is reasonably consistent and ranges 2% to 3.5%. There is no significant discrepancy found between the samples with Si_3N_4 powders and without Si_3N_4 powders in terms of dimensional errors for the sintered samples.

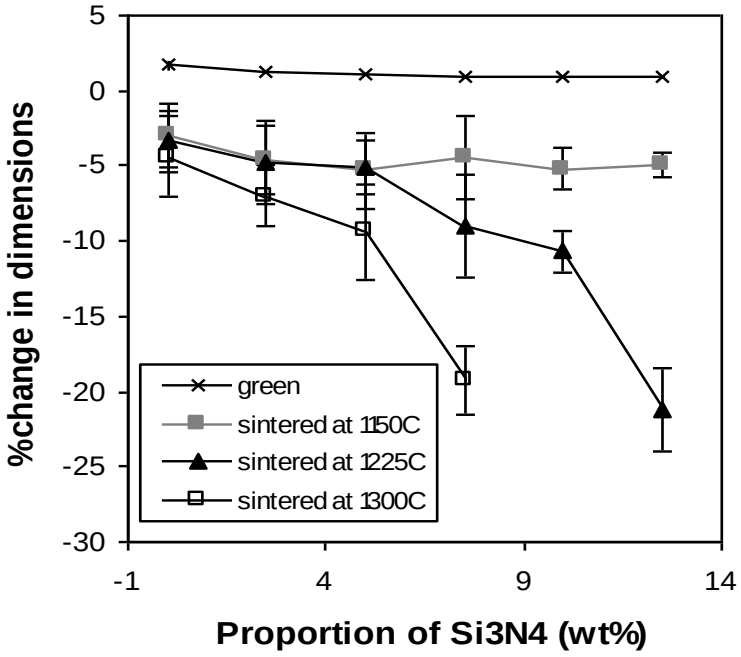

Figure 5.2.1-1. Shrinkage % in dimensions of green and sintered samples sintered at various temperatures (error bars indicate the standard deviation of the data points).

To quantify the degree of shape maintenance, the angles between two arms were also measured for each L-shaped sample. The angles of the green L-shaped samples were measured to be 90 ± 0.2^{o}. Due to the complete liquid sintering, the shapes of the samples with Si_3N_4 of 15 wt% sintered at $1225^{o}C$, and the samples with Si_3N_4 of 10, 12.5, and 15wt% sintered at $1300^{o}C$ were totally distorted. The angles of these samples have deviated substantially from those of the original samples. However, the angles of all the other sintered samples are within a small range from 89.7 to 93.5^{o}. For those samples shown in Fig. 5.2.1-2, the angle continuously increases as Si_3N_4 content increase for the samples with 0 to 7.5wt% Si_3N_4. Then the angle begins to decrease when the Si_3N_4 increase in further. The angle is almost the same to the corresponding green sample for the sintered samples with 12.5wt% Si_3N_4.

Two factors contributing to the shape-maintenance of the samples are liquid sintering and the pinning mechanism of second phase – Si_3N_4. The former obviously distorts the shape, while the later prevents the deformation. Transient liquid happens because of the addition of Si_3N_4. As Si_3N_4 increases, the beginning temperature of transient liquid sintering will decrease as mentioned in Section 3.3. Therefore, the liquid sintering temperature range gets wider, resulting larger shape change than the sample with lower Si_3N_4. However, once the proportion of the Si_3N_4 is beyond a threshold, the pinning mechanism of the second phase (Si_3N_4) will dominate the shape change. The presence of second phase in the matrix retards the migration of the grain boundary[63] to prevent the deformation. From the observation, the threshold of Si_3N_4 content should be between 7.5 to 10wt%. However, once the wt% of Si_3N_4 is over than 12.5wt%, total liquid sintering happens, resulting in distortion of the samples.

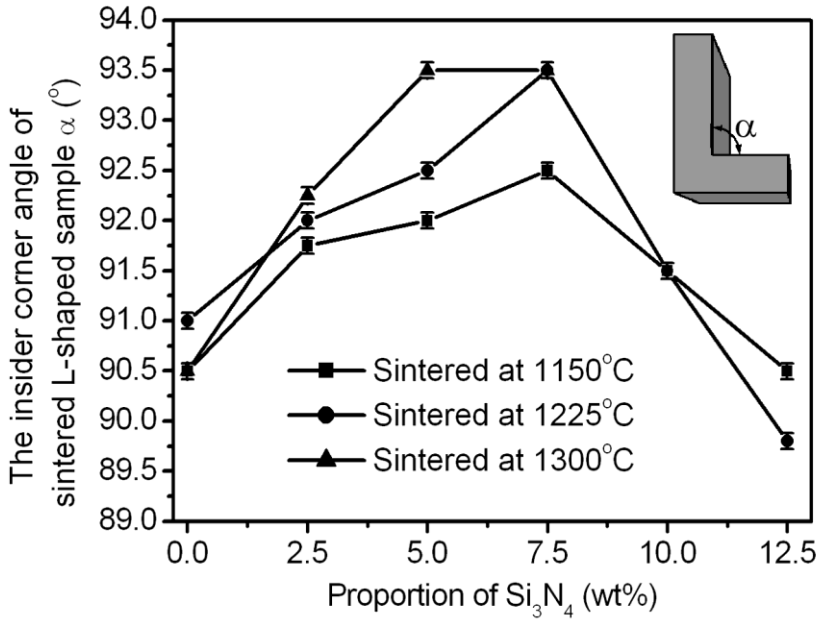

Figure 5.2.1-2. Angle variation of the inside corners for the various L-shaped samples (Soak duration: 6 hrs).

5.2.2 DIMENSIONS PERPENDICULAR TO THE BUILD PLATFORM

Dimensional change in the vertical direction or the Z direction is experimentally investigated using 8 mm cube samples. Unlike dimensional change parallel to the build platform, gravity is one of the factors affecting dimensional change in the vertical direction. We consider a specimen configuration as sketched in Fig. 5.2.2-1 to obtain information for the gravity-induced shape distortion during sintering. In order to describe the shape change, the ratio between the bottom width (l_s) and the top width (w_s) with respect to its initial value ($w_0/l_0 = 1$ for our samples) can be introduced. The sample's ratio close to 1 means the sample may not be distorted due to gravity during sintering.

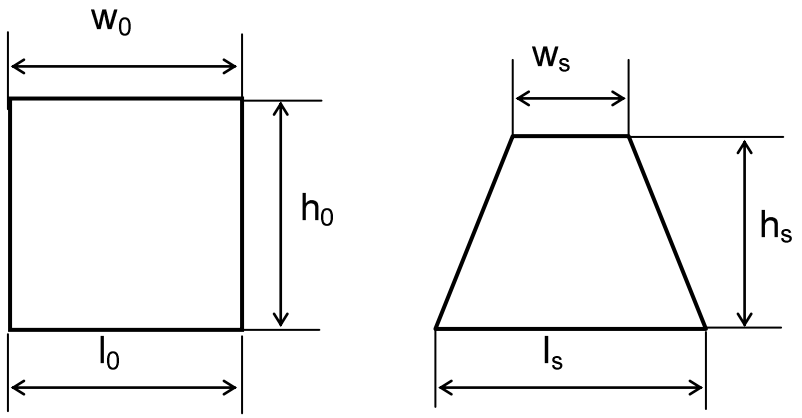

(a) CAD model (B) Sintered sample

Figure 5.2.2-1. CAD and sintered sample configurations.

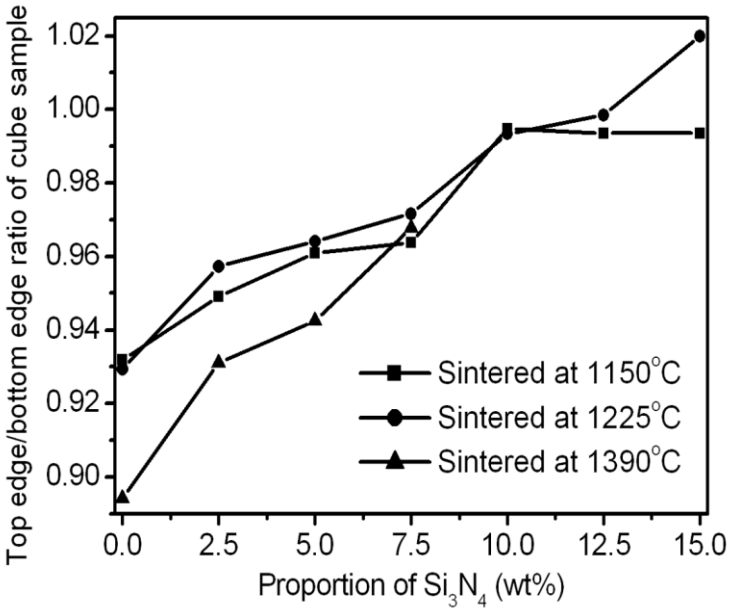

Figure 5.2.2-2 the Ratios of top width to bottom width for the sintered 3DP samples.

Fig. 5.2.2-2 shows the ratios of the top width (w_s) to the bottom width (l_s) with respect to its initial value of 1 for the samples with various Si_3N_4 contents and sintering temperatures. Data for the samples with 10, 12.5 and 15wt% of Si_3N_4 sintered at 1300ºC are missing due to their severe distortion during sintering. Without Si_3N_4, the ratio ranges 0.89 to 0.93. With increasing Si_3N_4 contents, the ratio increases to become close to 1. For example, the sample with 12.5 wt% Si_3N_4 sintered at 1225ºC shows the ratio of 0.99, which means the shape is conserved during the sintering process. This can be explained by the fact that greens with higher Si_3N_4 contents have larger green density before sintering. In addition, finer Si_3N_4 powders located gaps among SS powders may stabilize the shape of the samples during sintering.

5.2.3 EDGE QUALITY FOR THE 3DP PARTS

The edge quality of each sintered sample was measured using an SEM (Apex Inc., USA). Fig. 5.2.3-1 shows the SEM pictures of representative edges for each sample. Opposite to the results in dimensional change, dimensional accuracy of the edge contours increased with increasing Si_3N_4 wt% except the samples with 12.5 wt% and 15 wt% Si_3N_4 sintered at 1225ºC where liquid phase sintering was observed. This may be due to higher relative density or lower void contents of the green parts at higher Si_3N_4 contents. Without Si_3N_4 or lower contents of Si_3N_4, SS powders at the edges may collapse during sintering. Sample geometries can be stabilized with the existence of finer Si_3N_4 powders positioning among SS powders during sintering. Once liquid sintering occurs on the material system during sintering, sample edges can be distorted. Fig. 5.2.3-1 (f) shows very dull edge on the sample with 15 wt% Si_3N_4 sintered at 1225ºC.

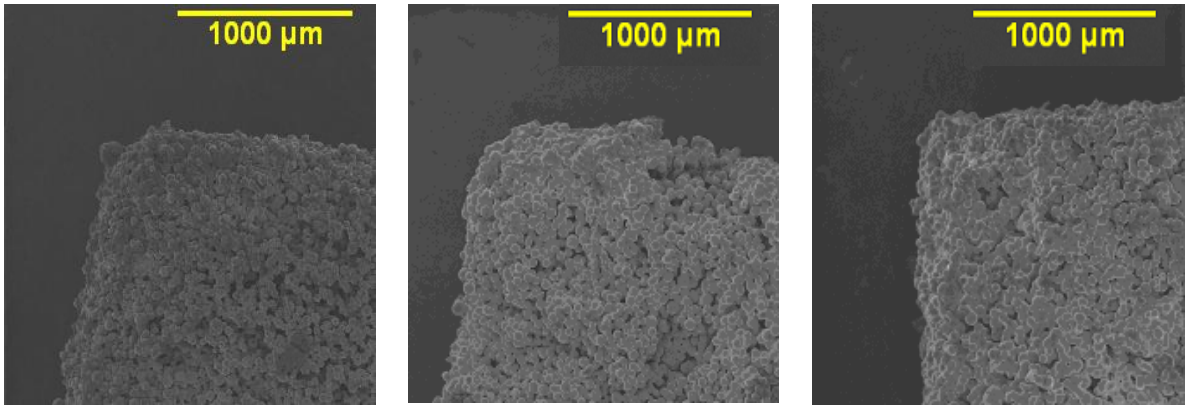

(a) 0 wt%　　(b) 5 wt　　(c) 7.5 wt%

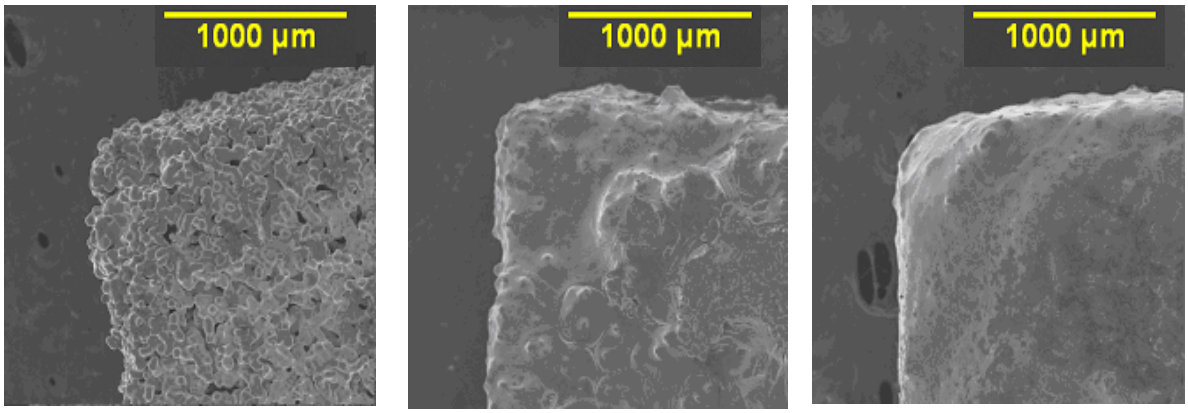

(d) 10 wt%　　(e) 12.5 wt%　　(f) 15 wt%

Figure 5.2.3-1 SEM pictures of the sintered 3dp sample edges with various wt% of Si_3N_4. (sintering temperature = 1225ºC)

5.3 MECHANICAL PROPERTIES

5.3.1 YOUNG'S MODULI OF SINTERED SAMPLES

Fig. 5.3.1-1 shows the tested Young's modulus of the sintered samples by three point bending method. The Young's modulus increases with higher sintering temperature or Si_3N_4 proportion. Young's modulus is generally proportional to the relative density. As mentioned before, both higher sintering temperature and increasing the Si_3N_4 proportion enhance the densification kinetics, resulting in the sample with a higher relative density and less porosity. From Fig. 5.3.1-1, The Young's modulus for both 12.5wt% Si_3N_4 sintered at 1225°C and 10wt% Si_3N_4 sintered at 1300°C are very close to the Young's modulus of 420 steel (~ 200GPa [50]).

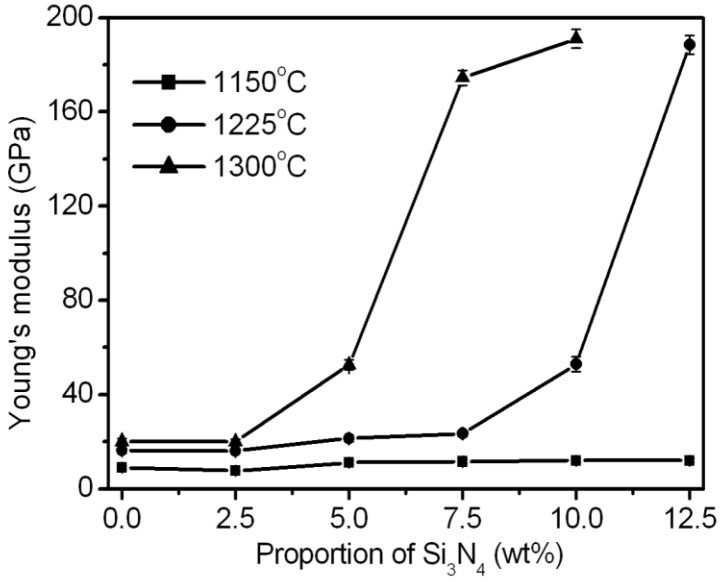

Figure 5.3.1-1. The Young's moduli of various samples (the 12.5 wt% Si_3N_4 samples sintered at 1300°C and most 15wt% Si_3N_4 samples are with smaller length than the supporter distance of three-point bending test supporters, so the corresponding result was not measured)

5.3.2 HARDNESS OF SINTERED SAMPLES

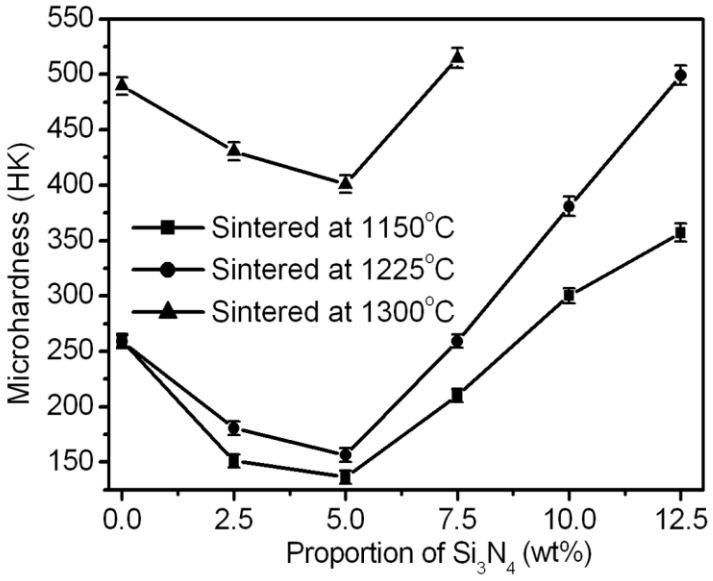

Figure 5.3.2-1. The microhardness of various samples (Samples with liquid sintering were not tested).

The measured hardness is reported in Fig. 5.3.2-1 for various sintered samples. As discussed before, only about 4wt% Si_3N_4 is dissolved into the 420 SS during the sintering process. Therefore, the samples with 0-5wt% Si_3N_4 are nearly without second-phased Si_3N_4 appearing at the SS boundaries. However, as Si dissolves in stainless steel, the carbon separates out from the Fe, causing Fe_3C decrease, which is the hardening phase. [64]. Also due to only around or less than 4wt% Si_3N_4 dissolved into 420 SS, the atom ratio between dissociative Si and Fe in the material system is less than 10%. Therefore, the Fe and dissociative Si are only bonded as Fe-Si diffusion couples, not the hardening phase, Fe_3Si [65]. These two alloy processes result in the hardness decrease as Si_3N_4 content increases for the samples with 0-5wt% Si_3N_4. Once the Si_3N_4 content is higher than 5wt%, the second phase hardening happens, resulting in the increased hardness. However, due to the size of Si_3N_4 being smaller than the diameter of the indenter,

extremely high hardness values were not obtained for the samples with Si_3N_4 content higher than 5wt% despite of the multiple measurements.

CHAPTER SIX

CONCLUSIONS

The 3DP process was used to manufacture high dense stainless steel part with addition of Si_3N_4. The effect of Si_3N_4 contents and sintering conditions on the density, dimensional change, hardness, and Young's modulus were studied experimentally. Based on the results the following conclusions were made:

1) Microstructures of green samples and volume proportion of each component of green samples varied as Si_3N_4 proportion changed.
2) Relative density and dimension of the sintered samples also varied in relation to the Si_3N_4 content and the sintering temperature. Si_3N_4 can effectively improve the densification kinetics of 420 SS at least to 15 wt% proportion, resulting in a higher density than pure 420 SS samples. Due to the pinning mechanism of second phase, Si_3N_4 phase, the better shape maintenance capability is obtained for samples with 10-12.5 wt% Si_3N_4. However, further increasing Si_3N_4 will cause fully liquid sintering and distorted the shape.
3) Young's modulus values increased as the density of samples increased due to the change in the sintering condition. Variations of micro-hardness values depending on Si_3N_4 contents and sintering conditions were analyzed.
4) Shrinkage in the direction parallel to the build platform increases with increasing Si_3N_4 contents and sintering temperature. However, dimensional errors of the samples with Si_3N_4 are similar to those without Si_3N_4.
5) With increasing Si_3N_4 contents, the vertical distortion of the samples during sintering can be minimized. Si_3N_4 powders located gaps among SS powders may stabilize the shape of the samples during sintering.

6) In general, existence of Si_3N_4 powders on the material system improved edge quality of the sintered parts except the samples showed liquid phase sintering.

7) The combination of 3DP method and optimal sintering condition had a high potential for obtaining uniform and dense SS parts. From the final density, the shape-maintenance capability as well as the mechanical properties, the optimal experimental factors are 12.5wt% Si_3N_4 content, 1225^oC sintering temperature, and 6 hours soak duration for the 420 SS samples.

8) The result of the research was novel in terms of developing new material system for 3DP technique to overcome drawbacks caused by low relative density of final parts. This research showed the possibility of fabricating high-dense stainless steel parts with shape maintenance capability.

9) Further researches for practical or industrial applications of this research results are needed. One possible application of this research result could be fabricating small numbers of complex stainless gear parts. This is because in order to fabricate gear parts by conventional powder metallurgy method, manufacturing tools are needed and tooling is suitable for mass production, not for customized production. Therefore, by using 3DP technique with new material system developed by this research, it would be possible to fabricate such kinds of complex stainless gear parts or other complex parts for different applications by individual and occasional demands.

BIBLIOGRAPHY

[1] P.F. Jacobs, Rapid prototyping and Manufacturing: Fundamentals of Stereo-lithography, Society of Manufacturing Engineers, ISBN 978-0070324336 (1992)

[2] J. Giannatsis, and V. Dedoussis, Additive fabrication technologies applied to medicine and health care: a review, International Journal of Manufacturing Technology, 40 (2009) 116-127

[3] J.G. Conley, and H.L. Marcus, Rapid Prototyping and Solid Freeform Fabrication, Journal of Manufacturing Science and Engineering, 119 (1997) 811-816

[4] S. Johnston, R. Anderson, and D. Storti, Sintering Strain of 316L Stainless Steel Parts Fabricated by Three-Dimensional Printing, Transactions of the NAMRI/SME, 34 (2006) 499-506

[5] H. Kakisawa, K. Minagawa, K. Ida, K. Maekawa, and K. Halada, Dense P/M Component Produced by Solid Freeform Fabrication, Journal of Materials Transactions, 46/12 (2005) 2574-2581

[6] S.M Allen, and E.M. Sachs, Three-Dimensional Printing of Metal Parts for Tooling and Other Applications, Metal and Materials, 6/6 (2000) 589–594

[7] W.Y. Yeong, C.K. Chua, K.F. Leong, and M. Chandrasekaran, Rapid prototyping in tissue engineering: challenges and potential, Trends in Biotechnology, 22/12 (2004) 643-652

[8] Q. Liu, M.C. Leu, and S.M. Schmitt, Rapid prototyping in dentistry: technology and application, International Journal of Advanced Manufacturing Technology, 29 (2006) 317-335

[9] C.W. Hull, Apparatus for production of Threre-Dimensional Objects by Stereolithography, UVP Inc. U.S patent 4575330 (1986)

[10] B.J. Tay, J.R.G Evans, and M.J. Edrisinghe, Solid freeform fabrication of ceramics, International Materials Reviews, 48/6 (2003) 341-370

[11] M.L. Griffith and J.W. Halloran, Freeform Fabrication of Ceramics via Stereolithography, Journal of American Ceramic Society, 79/10 (1996) 2601- 2608

[12] D.T. Pham, and R.S. Gault, A comparison of rapid prototyping technologies, International Journal of Machine Tools and Manufacture, 38 (1998) 1257-1287

[13] Setreolithography applications, available at: http://louisville.edu/speed/rpc/SLAapp.htm

[14] B. Wendel, D. Rietzel, F. Kuhnlein, R. Feulner, G. Hulder, and E. Schmachtenberg, Additive Processing of Polymers, Macromolecular Materials and Engineering, 293 (2008) 799-809

[15] S. Singare, G. Lian, W.P. Wang, J. Wang, Y. Liu, D. Li, and B. Lu, Rapid prototyping assisted surgery planning and custom implant design, Rapid Prototyping Journal, 15 (2009) 19-23

[16] M. Schuster, C. Turecek, F. Varga, H. Lichtenegger, J. Stampfl, and R. Liska, 3D-shaping of biodegradable photopolymers for hard tissue replacement, Applied Surface Science, 254 (2007) 1131-1134

[17] A. Bertsch, P. Bernhard, C. Vogt, and P. Renaud, Rapid prototyping of small size objects, Rapid prototyping Journal, 6/4 (2000) 259-266

[18] J.W. Lee, P.X. Lan, B. Kim, G. Lim, and D.W. Cho, 3D scaffold fabrication with PPF/DEF using micro-stereolithography, Microelectronic Engineering, 84 (2007) 1702-1705

[19] J.Y. Kim, J.W. Lee, S.J. Lee, E.K. Park, S.Y. Kim, D.W. Cho, Development of a bone scaffold using HA nanopowder and micro-stereolithography technology, Microelectronic Engineering 84 (2007) 1762-1765

[20] Z. Zhou, D. Li, J. Zeng, and Z. Zhang, Rapid fabrication of metal-coated composite stereolithography parts, Journal of Engineering Manufacture 221 (2007) 1431-1440

[21] C.K. Chua, K.F. Leong, and C.S. Lim, Rapid Prototyping: Principles and Applications, World Scientific Books, ISBN 978-9812778987 (2003)

[22] W. Zeng, F. Lin, R. Shi, R. Zhang, T. Nian, J. Ruan, and R. Zhou, Fused deposition modeling of an auricle framework for microtia reconstruction based on CT images, Rapid Prototyping Journal 14/5 (2008) 280-284

[23] E. Kouhi, S. Masood, and Y. Morsi, Design and fabrication of reconstructive mandibular models using fused deposition modeling, 28/3 (2008) 246-254

[24] A. Yamada, F. Niikura, and K. Ikuta, A three-dimensional microfabrication system for biodegradable polymers with high resolution and biocompatibility, Journal of Micromechanics and Microengineering, 18 (2008) 1-9

[25] SJ. Kalita, S. Bose, HL. Hosick, and A. Bandyopadhyay, Development of controlled porosity polymer-ceramic composite scaffolds via fused deposition modeling, Materials Science and Engineering C-Biomimetic and Supramolecular, 23/5 (2003) 611-620

[26] S. Finke, and F.K. Feenstra, Solid freeform fabrication by extrusion and deposition of semi-solid alloys, Journal of Materials Science, 37 (2002) 3101-3106

[27] M. Allahverdi, A. Hall, R. Brennan, M.E. Ebrahimi, N.M. Hash, and A. Safari, Processing of advanced electroceramic components by fused deposition technique, Journal of the European Ceramic Society, 21 (2001), 1485-1490

[28] H. Meier, and C. Haberland, Experimental studies on selective laser melting of metallic parts, Mat.-wiss. u. Werkstofftech. 39/9 (2008) 665-670

[29] J.P. Kruth, P. Mercelis, and J.V. Vaerenbergh, Binding mechanisms in selective laser sintering and selective laser melting, Rapid Prototyping Journal, 11/1 (2005) 26-36

[30] F. Collins, EuroMold 2000 to Feature Roger Spielman of Boeing's Rocketdyne, Euro Mold 2000 Conference, 1 December, 2000, Frankfurt, Germany

[31] A.T. Clare, P.R. Chalker, S. Davies, C.J. Sutcliffe, and S. Tsopanos, Selective laser melting of high aspect ratio 3D nickel-titanium structures two way trained for MEMS applications, International Journal of Mechanical Design, 4 (2008) 181-187

[32] I. Yadroitsev, I. Shishkovsky, P. Bertrand, and I. Smurov, Manufacturing of fine-structured 3D porous filter elements by selective laser melting, Applied Surface Science, 255 (2009) 5523-5527

[33] Y.F. Shen, D.D. Gu, and P. Wu, Development of porous 316L stainless steel with controllable microcellular features using selective laser melting, Materials Science and Technology, 24/12 (2008) 1501-1505

[34] M.M. Savalani, L. Hao, Y. Zhang, K.E. Ranner, and R.A. Harris, Fabrication of porous bioactive structures using the selective laser sintering technique, Proceedings of the Institution of Mechanical Engineering Part H – Journal of Engineering in Medicine, 221/8 (2007) 873-886

[35] E. Sachs, M. Cima, P. Williams, D. Brancazio, and J. Cornie, Theee-dimensional printing: rapid tooling and prototypes directly from a CAD model, Transaction of the ASME, Journal of Engineering for Industry, 114 (1992) 481-488

[36] D. Bak, Rapid prototyping or rapid production? 3D printing processes move industry towards the latter, Assembly Automation, 23/4 (2003) 340-345

[37] D. Dimitrov, K. Schreve, and E. Bradfield, Accelerated development of plastic components for automotive applications, paper presented at Plasmobile Conference, 22-23 October, 2002, Johannesburg.

[38] D. Dimitrov, K. Schreve, and N.D. Beer, Advances in three dimensional printing – state of the art and future perspectives, Rapid Prototyping Journal, 12/3 (2006) 136 - 147

[39] W. Sun, D.J. Dcosta, F. Lin, and T. EI-Raghy, Freeform fabrication of Ti_3SiC_2 powder-based structures Part 1 – Integrated fabrication process. Journal of Materials Processing Technology, 127 (2002) 343-351

[40] T. El-Raghy, and M.W. Barsoum, Synthesis and characterization of a remarkable ceramic: Ti_3SiC_2, Journal of American Ceramic Society, 79/7 (1999) 1653-1658

[41] T. El-Raghy, and M.W. Barsoum, Processing and mechanical properties of Ti_3SiC_2, Part 1: reaction path and microstructure evolution, Journal of American Ceramic Society, 82 (1996) 1953-1956

[42] J.B. Kaczynski, Three dimensional printing – any composition, any material, any geometry, Research Program, available at: http://web.mit.edu/tdp/www

[43] A. Lorenz, E. Sachs, and S. Allen, Freeze-Off Limits in Transient Liquid-Phase Infiltration, Metallurgical and Materials Transactions, 35A (2004) 641-653

[44] A. Lorenz, E. Sashs, S. Allen, L. Rafflenbeul, and B. Kernan, Densification of a Powder-Metal Skeleton by Transient Liquid-Phase Infiltration, Metallurgical and Materials Transactions, 35A (2004) 631-640

[45] M. Koizumi, and M. Nishihara, Isostatic Pressing: Technology and applications, Elsevier Applied Science, ISBN 978-1851665969 (1991)

[46] J. Sicre-Artalejo, F. Petzoldt, M. Campos, and J.M. Torralba, High-density Inconel 718m: Three-dimensional Printing Coupled with Hot Isostatic Pressing, International Journal of Powder Metallurgy, 44/1 (2008) 35-43

[47] H.V. Atkinson and S. Davies, Fundamental Aspects of Hot Isostatic Pressing: An Overview, Metallurgical and Materials Transactions A, 31A (2000) 2981-2998

[48] D. Godlinski, H. Pohl, and S. Morvan, Rapid manufacturing of dense stainless steel parts by 3D-printing, Proceedings of European Conference on Powder Metallurgy Euro PM2005, (2003) 61-65

[49] M. Lanzetta and E. Sachs, Improved surface finish in 3D printing using bimodal powder distribution, Rapid Prototyping Journal, 9/3 (2003) 157 – 166

[50] K.G. Budinski, and M.K. Budinski, Engineering Materials: Properties and Selection, 6th edition, Prentice Hall, ISBN 0-13-904715-8 (1999)

[51] L. Sun, P. Kwon, D. Kim, and K. Beavers, Progress Toward a Denser Metal Matrix Composite using the Three Dimensional Printing Method, Transactions of the NAMRI/SME, 36 (2008) 105-112

[52] R.M. German, Powder metallurgy science, 2nd edition. Metal Powder Industries Federation, ISBN 978-1878954428 (1994)

[53] M. Barsown, Fundamental of Ceramics, McGraw-Hill Companies, ISBN 978-0070055216 (1996)

[54] M.I. Jones, M.C. Valecillos, and K. Hirao, Densification Behavior in Microwave-Sintered Silicon Nitride at 28 GHz, Journal of the American Ceramic Society, 84/10 (2001) 2424-2426

[55] R.L. Coble, Sintering Crystalline Solids. 1. Intermediate and Final State Diffusion Models, Journal of Applied Physics, 32 (1961) 787-792

[56] M. Lindholm, A Thermodynamic Description of the Fe-Cr-Si System with Emphasis on the Equilibria of the Sigma(σ) Phase, Journal of Phase Equilibria, 18/5 (1997) 432-440

[57] Z. Zhang, and R. Sandstrom, Fe-Mn-Si Master Alloy Steel by Powder Metallurgy Processing, Journal of Alloys and Compounds, 363 (2004) 194-202

[58] A. Farid, P. Feng, X. Du, A.S. Jawid, J. Tian, and S. Guo, Microstructure and Property Evolution during the Sintering of Stainless Steel Alloy with Si_3N_4, Journal of Materials Science and Engineering A. 472 (2008) 324-331

[59] Y.C. Chen, C. Iwamoto, and Y. Ishida, Chemical Behavior on Diffusion Bonding of Si_3N_4-Ni and Si_3N_4-superalloy IN-738, Scripta Materialia, 35/6 (1996) 675-681

[60] R. Jones, V. Randle, and G. Owen, Carbide Precipitation and Grain Boundary Plane Selection in Overaged Type 316 Austenitic Stainless Steel, Materials Science and Engineering A, 496 (2008) 256-261

[61] L.V. Tarasenko, Rules of Formation of the Chemical Composition of $M_{23}C_6$ Multicomponent Carbide in High-temperature Steels, Metal Science and Heat Treatment, 42/1 (2000) 6-10

[62] N. Hopkinson, Process repeatability and sources of error in indirect SLS of aluminium, Rapid Prototyping Journal, 14/2 (2008) 108-113

[63] K. Song, and M. Aindow, Grain Growth and Particle Pinning in a Model Ni-based Superalloy, Materials Science and Engineering A, 479 (2008) 365-372

[64] K. Sanbongi, M. Ohtani, and K. Toita, K, On the Effect of Alloying Elements on the Solubility of Carbon in Molten Iron, Science Report of the Research Institutes at Tohoku University in Japan, 9 (1957) 147-158

[65] Y. Zhang, and D.G. Ivey, Fe_3Si Formation in Fe-Si Diffusion Couples, Journal of Materials Science, 33 (1998) 3131-3135

[66] D. Szabo, and M. Schneebeli, Subsecond Sintering of Ice, Applied Physics Letter, 90:151916 (2007)

[67] K. Lu, and W.T. Reynolds, 3DP process for fine mesh structure printing, Powder technology, 187 (2008) 11-18

[68] L. Lu, M. Hiser, and W. Wu, Effect of particle size on three dimensional printed mesh structures, Powder Technology, 192 (2009) 178 – 183

[69] R.A. Giordano, B.M. Wu, S.W. Borland, L.G. Cima, E.M. Sachs, and M.J. Cima, Mechanical properties of dense polyactic acid structures fabricated by three dimensional printing, Journal of Biomateiral Science and Polymer Engineering, 8/1 (1996) 63 – 75

[70] M. Youseffi, M., and K.Y. Chong, Enhanced Sintering and Mechanical Properties of 316L Stainless Steel with Silicon Additions as Sintering Aid, Powder Metallurgy, 46/1 (2003) 30-38

Appendix

FABRICATION OF METAL PARTS WITH MICRO-SIZED HOLES

Three dimensional metal parts with micro-sized holes, as shown in Fig. A-1. were fabricated by 3DP technique and determining optimum 3DP process parameters was performed by two sets of design of experiment (DOE) method as shown in Table A-1 and Table A-2.

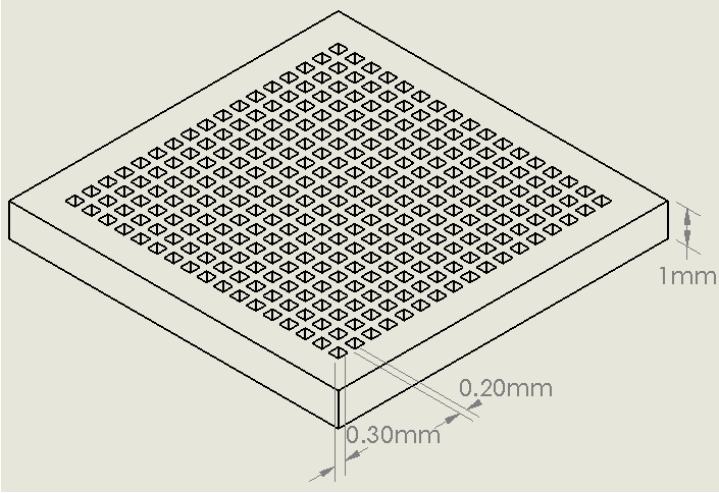

Figure A-1. Schematic of metal parts with micro-sized holes

The purpose of the fist DOE was screening 3DP process parameters to determine whether each 3DP process parameter is influential for the final feature of metal structures.

Table. A-1. The first DOE set for screening process parameters

Run	Feature thickness(mm)	Saturation %	Drying time(sec)	Layer thick(μm)	Fail/OK	Closed hole #	De-lamination
1	2	35	10	100	OK	17%	No
2	1	25	10	100	OK	3%	No
3	1	35	10	250	OK	7%	Yes
4	1	25	40	250	OK	3%	Yes
5	2	25	40	100	Fail		
6	2	35	40	250	OK	33%	Yes
7	1	35	40	100	OK	3%	No
8	2	25	10	250	Fail		

From the result of the first DOE set, it was found that drying time was not influential factor for the final sample features, and layer thickness of 250 μm caused de-lamination of samples. From the results of the first DOE, for the second DOE test, drying time of 20 second, which is given from the 3DP manufacturer, was used as a fixed process parameter because of its less influence, and layer thickness of 100 μm was used since too thick layer thickness caused de-lamination effect. Feature thicknesses were varied from 1mm to 2mm with an interval of 0.5mm, and binder saturation used were 25%, 35%, and 45% to determine a set of optimum process parameters for an ideal fine mesh structure. Fig. A-2 and Fig. A-3 are graphical expression of Table A-1.

Table. A-2. The results of the second DOE set

Run	Feature thickness(mm)	Saturation%	Drying time	Layer thick	Fail/OK	Hole size(um)	Gap size(um)	Closed hole #
1	1	25	20	100	OK	274	226	7%
2	1.5	25	20	100	OK	247	253	27%
3	2	25	20	100	OK	245	255	43%
4	1	35	20	100	OK	264	236	7%
5	1.5	35	20	100	OK	238	262	10%
6	2	35	20	100	OK	237	263	17%
7	1	45	20	100	OK	194	306	17%
8	1.5	45	20	100	OK	192	308	23%
9	2	45	20	100	OK	190	310	33%

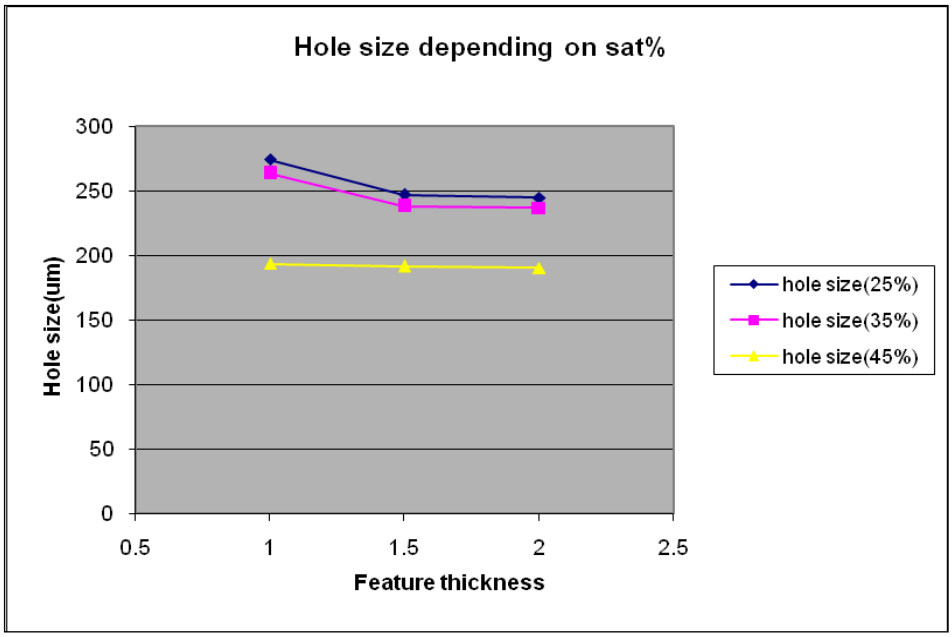

Figure A-2. Hole size evaluation depending on feature thickness and saturation%

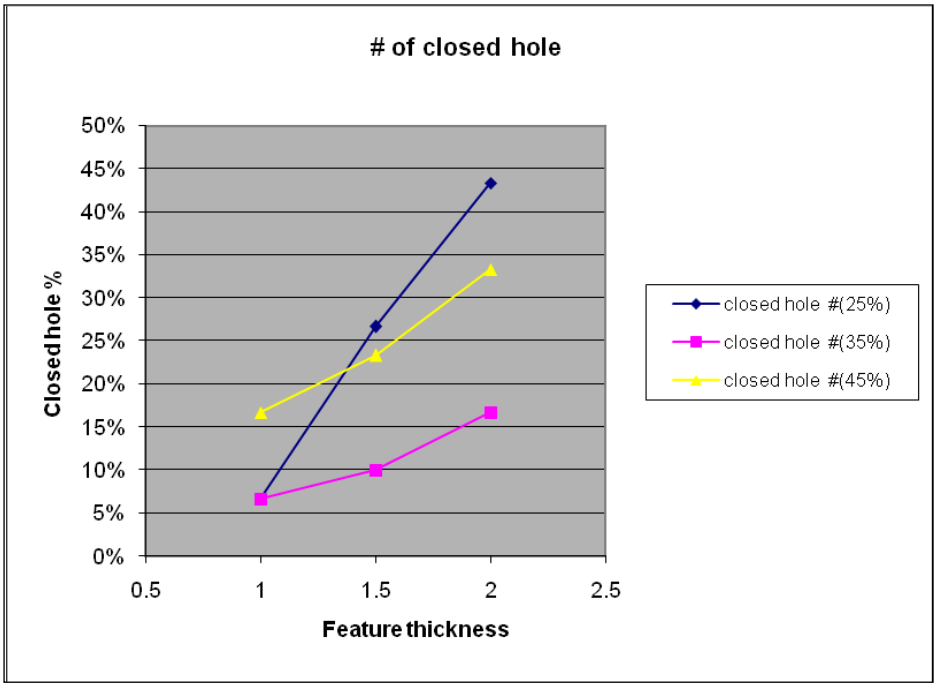

Figure A-3. The number of closed holes evaluation depending on feature thickness and saturation%

It is observed that hole sizes decreased as feature thickness and saturation% increased as shown in Fig. A-2. This is because for the sample with higher feature thickness (high aspect ratio), it was hard to remove powder debris from the holes, causing decrease of hole sizes. Furthermore, higher saturation% make the structure thick, which also cause decrease of hole sizes.

For the evaluation of the number of closed holes, for the sample with saturation% of 35% and 45%, it had opposite trends to the hole size evaluation that the number of closed holes increased as feature thickness and saturation% increased, since the sample with higher aspect ratio and higher saturation%, it was hard to get rid of powder debris from the holes, causing increase of the number of closed hole. However, for the samples with saturation% of 25%, because of the weak green strength, impacting green samples to remove the support powder in the holes was difficult. That caused the increase of the number of closed holes for the samples with saturation% of 25%, even though the saturation% decreased. Exceptionally, for the sample with feature thickness of 1mm and saturation% of 25%, low aspect ratio made it possible to remove the support powders from the holes without breaking the green samples, causing very small number of closed holes.

From the result of the second DOE, based on the hole size and the number of closed hole evaluation, it was found that for the sample with saturation% of 35% and feature thickness of 1mm yield the best result for the metal parts fabrication with micro-sized holes.

PREPARATION OF SS POWDER WITH CARBON NANOTUBE (CNT) DEPOSITED

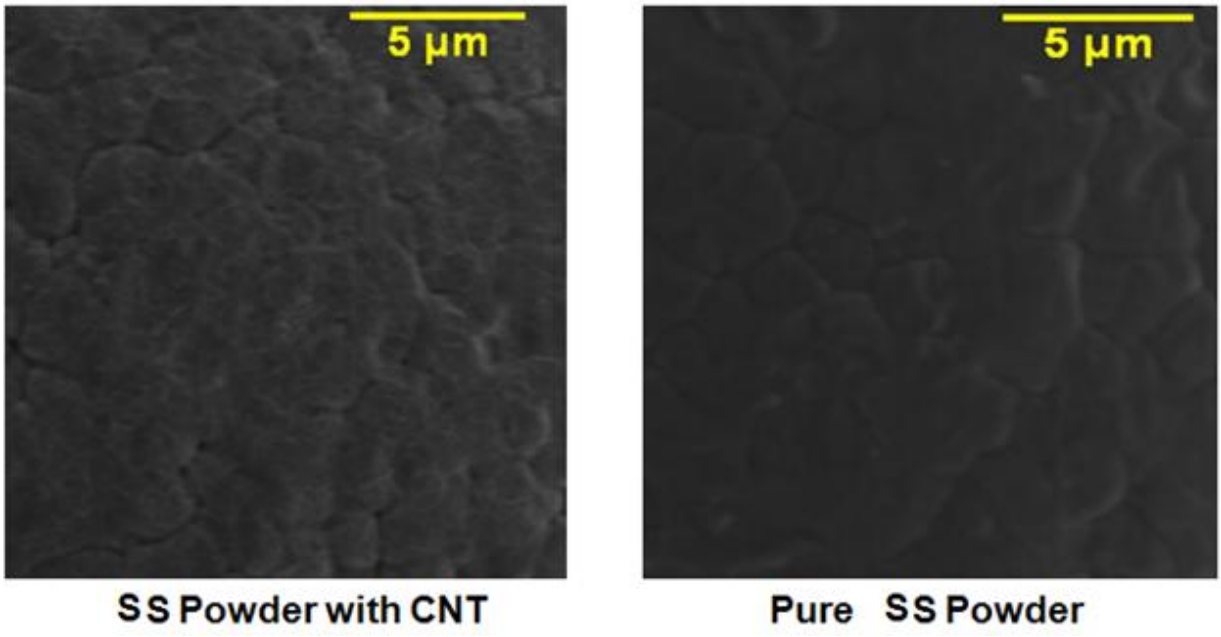

Figure A-4. SS powder with CNT (left) and without CNT (right)

CNT solution preparation: Density of 1mg/1ml – Provided by Prof. Wei Xue

(W. Xue, and T. Cui, Carbon nanotube micropatterns and cantilever arrays fabricated with layer-by-layer nano self-assembly, Sensors and actuators A 136 (2007) 510-517)

a. Chemically Functionalization:

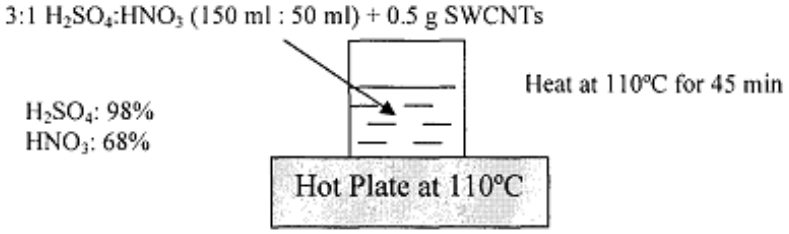

b. Dilute the $H2_SO_4$:HNO_3 solution to 500 ml.
Add acid to water!

c. Filter the functionalized SWCNTs from the acid
Millipore Stericup / Steritop Filter Unit
https://www1.fishersci.com/Coupon?cid=1341&gid=105603

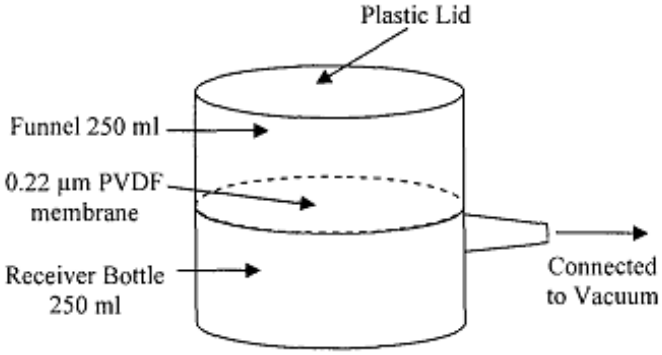

d. Clean the functionalized SWCNTs using DI water for several (5-10) times
Detect the pH value, until the pH value approaches 5.

e. Ultrasonic vibration
500 ml water + 0.5 g functionalized SWCNT in ultrasonic for about 1 hour.

f. Centrifuge (if necessary or before use)
To remove the SWCNT bundles and some long SWCNTs.
5000 rpm for 15 min.

3DP System maintenance

Sponge Wiper replacement

1. This instruction will cover the removal and installation of the sponge wiper.
    a. The sponge wiper should be replaced –
        i. On a weekly basis
        ii. Or if the wiper has tears or gouges on the surface.
        iii. Or if the wiper has powder contamination that may impact the printhead performance.

2. Materials:
    a. Sponge wiper *imagen* part number 3300182.
    b. Metric Allen wrench – 2.5mm.

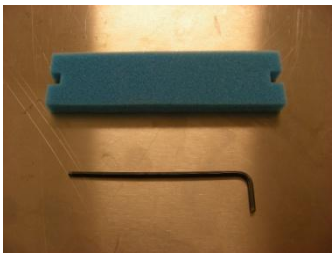

3. Remove the retainer:
    a. Remove the two screws on each end of the wiper retainer.
    b. Lift the retainer from the wiper and clean thoroughly.

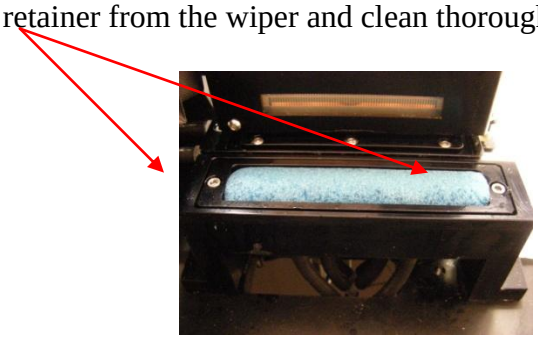

4. Remove the old wiper:
    a. Lift the wiper out of the trough.
    b. The wiper may tear in some places due to dried binder on the walls or corners of the trough.
    c. Using cleaner or alcohol, wet any pieces of sponge that remain, then remove them with a little rubbing action using a paper towel.

5. Prepare the new sponge wiper:
    a. The new wipers have a slot cut at each end for retaining screw clearance.
        i. The wiper ends must be trimmed to fit just inside the retainer inner edges.

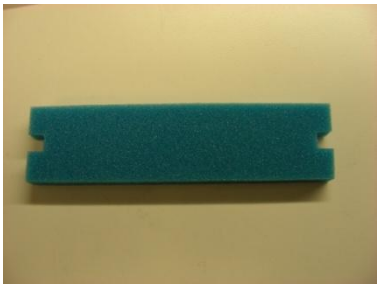

    b. Place the wiper on a flat surface.
    c. Place the cleaned retainer on top of it so that ends align.

    d. With a ballpoint pen, mark the sponge at the “inside” of each end of the retainer.

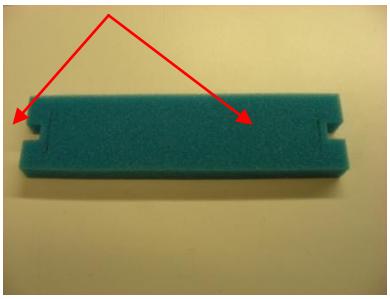

    e. Using a pair of sharp scissors, cut the ends at the lines.
        i. Using dull scissors will cause the cut ends to crimp and now work properly.

f. Install the new sponge wiper:
g. Place the shortened wiper into the wiper station trough centered as best as possible.

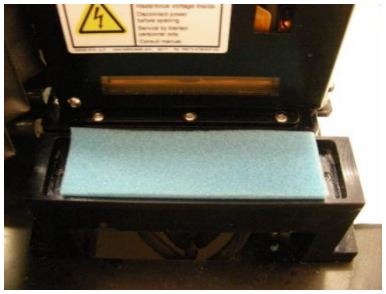

h. Place the retainer over the wiper so that the retaining screw holes align.
    i. Both ends of the wiper must fit inside the retainer. If this is not the case, reposition the wiper.

i. Once positioning is correct, hold the retainer flat with one hand and install the retaining screws, tightening them alternately to put even pressure on the sides of the sponge wiper.
j. Each edge of the wiper will protrude slightly at the ends of the retainer.

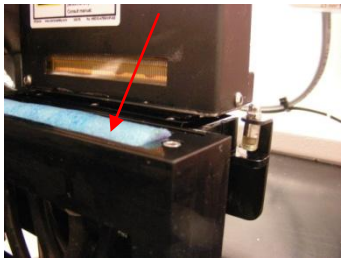

6. Wet the wiper:
    a. From the Printhead Setup and Test screen, perform 2 “clean wiper” cycles.
    b. Wipe the top of the sponge wiper with your finger to make sure cleaner saturates the entire surface.

7. The printer is ready for use.

Checking vent valve

a. The vent valve is located at the rear of the Y axis.

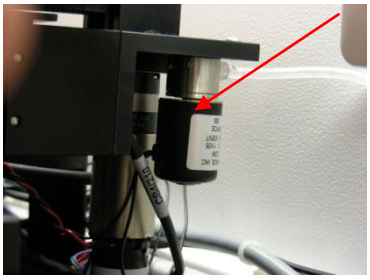

- Remove clear tubing going to valve
- Attach another piece of tubing to barb fitting on valve
- With valve open see if you can blow air through valve
- With valve shut verify you cannot blow air through valve
- Trim back ¼ inch of original tubing and re connect to valve